Journal of Solid State Chemistry **145,** 401–420 (1999)
Article ID jssc.1999.8111, available online at http://www.idealibrary.com on IDEAL®

Evolution of the Structure of the K_2NiF_4 Phases $La_{2-x}Sr_xNiO_{4+\delta}$ with Oxidation State: Octahedral Distortion and Phase Separation ($0.2 \leq x \leq 1.0$)

J. E. Millburn,* M. A. Green,*,[1] D. A. Neumann,† and M. J. Rosseinsky*

*Inorganic Chemistry Laboratory, Department of Chemistry, University of Oxford, South Parks Road, Oxford, OX1 3QR, United Kingdom; and †National Institute for Standards and Technology, Centre for Neutron Research, Gaithersburg, MD 20899

Received September 4, 1998, in revised form November 10, 1998; accepted November 22, 1998

The structural properties of the $La_{2-x}Sr_xNiO_{4+\delta}$ solid solution have been investigated by high resolution powder neutron diffraction as a function of Sr dopant concentration. There is a significant change in the evolution of the shape of the NiO_6 octahedron beyond $x = 0.6$, where previous transport measurements have indicated a transition in the electronic structure. For the $x = 1$ member of the series prepared under conditions often adopted in the literature, a subtle inhomogeneity is visible in the high-resolution powder diffraction patterns and interpreted as arising from a distribution of La/Sr ratios throughout the sample under these widely used preparative conditions. The refined model, incorporating both strain broadening and Bragg peak displacement, can be interpreted as a continuum of phases with differing *c*, but similar *a*, lattice parameters. Preparation of $LaSrNiO_{4+\delta}$ at 1450°C appears to overcome this effect but Rietveld refinement is only possible with the aid of *hkl* dependent line broadening analysis, in contrast to the other members of the series studied.

INTRODUCTION

The Ni^{II}/Ni^{III} $La_{2-x}Sr_xNiO_{4+\delta}$ oxides with the K_2NiF_4 structure have been the focus of much recent research (1–10) in order to understand the very pronounced differences in electronic behavior from the isostructural high temperature superconducting copper oxides $La_{2-x}Sr_xCuO_4$ (11). Both families of oxides have a high degree of oxygen 2*p* character in the formally metal 3*d*-derived valence band, although band structure calculations indicate the 3*d* band is narrower and contains less O 2*p* character in the nickelate (12, 13). The electronic structures evolve in a quite different way on oxidation from the divalent metal. La_2NiO_4 and La_2CuO_4 are antiferromagnetic insulators with the layered K_2NiF_4 structure. In $La_{2-x}Sr_xCuO_{4\pm\delta}$ antiferromagnetic long-range order is replaced by short-range two-dimensional magnetic correlations for $x \geq 0.02$ (14), and the material becomes metallic and superconducting for $x \geq 0.06$ with the maximum transition temperature found for $x \sim 0.15$. Much higher doping levels are required to induce metal-insulator transitions in the $La_{2-x}Sr_xNiO_{4+\delta}$ series than in the analogous cuprates, with truly metallic behavior only occurring at nickel oxidation states higher than +III (2, 15). No superconductivity is observed. The aim of this paper is to investigate the structure and microstructure of the nickelate phases in detail in order to allow a chemical interpretation of the evolution of the electronic structure with oxidation state.

Transport measurements on the layered nickelates are consistent with a change in electronic ground state beyond $x = 0.5$–0.6, where the room temperature resistivity decreases sharply (2, 16). Samples with $x < 0.6$ undergo a sharp metal-insulator transition above 300 K and have similar resistivities at 300 K (1, 2). For $x = 0.5$–0.9, three-dimensional variable range hopping is observed ($5 \leq T/K \leq 300$), while $x = 0.9$ and 1.0 display weak localisation below 25 K, consistent with the upturn in resistivity below 100 K. Metallic behavior to 4 K is only established for $x > 1.1$ (2, 16–18). Seebeck and transport measurements indicate polaronic effects, with polaron binding energies of about 100 meV; the negative thermopower beyond $x = 0.8$ indicates the electron character of the charge carriers in the metallic state (3, 6). In the $La_{2-x}Sr_xNiO_4$ series, irreversible magnetism characteristic of a spin glass is observed for $x \leq 0.8$; i.e., before the metal-insulator transition (3). The $x = 0$ member of the series, $La_2NiO_{4\pm\delta}$, has been widely studied and is a spin = 1 antiferromagnet ($m = 1.68(6)\ \mu_B$ (19)) with a Néel temperature which depends very strongly upon the precise oxygen content ($T_N = 330$ K for $\delta = 0.0$ (19) decreasing to 75 K for $\delta = 0.10$ (20)). The magnitude of the magnetic susceptibility decreases with increasing *x*. For $x \approx 1$, the susceptibility is small in overall magnitude

[1]Current address: The Royal Institution of Great Britain, 21, Albemarle Street, London.

0022-4596/99 $30.00

compared to that observed for samples with low x and only weakly temperature dependent (2). However, recent muon spin relaxation measurements indicate that static magnetic order, albeit with a broader field distribution, persists up to $x = 1.0$, with a spin freezing temperature, T_M, of 44 ± 14 K (21). The approach to the metal-insulator transition therefore takes place without rapid suppression of magnetic order on oxidation, in contrast to the cuprates, and the correlation splitting of the e_g band remains to large values of x. Interestingly, these magnetic ordering temperatures are comparable to those of the cuprates although estimates of the intralayer Ni^{II}–Ni^{II} exchange coupling (of the order of 140 K) are an order of magnitude lower than the cuprates; this must reflect stronger interlayer coupling in the nickelates.

Renewed interest in the physical properties of the nickelates was stimulated by the observation of superlattice formation at $x = 0.33$ by electron diffraction below 235 K (5), coincident with resistivity, magnetisation (7), and heat capacity (22) anomalies. This was interpreted as the formation of an ordered array of polarons, reminiscent of the "charge ordering" phenomena currently of importance in manganese oxides displaying colossal magnetoresistance (23). Short-range (150 Å correlation length) spin and charge ordering has been observed by neutron diffraction in $La_{2-x}Sr_xNiO_{4.00}$ single crystals for $x = 0.125$, 0.20, 0.225 and 0.33 with spin ordering at 100 K occurring after charge ordering at 150 K at $x = 0.225$ (24, 25). Short-range magnetic ordering in the nickelates was, however, first identified by neutron powder diffraction in $Nd_{1.5}Sr_{0.5}NiO_4$ (26). The interpretation of neutron scattering measurements on $La_2NiO_{4+\delta}$ and $La_{2-x}Sr_xNiO_{4.00}$ is in terms of the formation of "stripes" of hole-rich domain walls separating domains of ordered spins (27), in line with theoretical predictions of the segregation of hole-rich regions due to the nonlinear variation of the energy per unit area with hole concentration (28).

Analysis of these recent measurements has focused exclusively on the nickel oxidation state without consideration of the orbital ordering or electronic configuration of the cation. The variation of the c/a ratio and X-ray powder diffraction-derived bond lengths has been interpreted in terms of Jahn–Teller distortion and configuration changes at the nickel (16), but sufficiently precise comparative structural data to test these ideas are not yet available. The localized or delocalized nature of the e_g electrons can be expected to strongly influence the occurrence of Jahn–Teller distortion at the Ni(III) centers introduced on oxidation. In this paper we present neutron powder diffraction data on the $La_{2-x}Sr_xNiO_4$ series for $0.2 \leq x \leq 1.0$. Previous structural studies at room temperature, using powder and single crystal X-ray diffraction, upon members of the $La_{2-x}Sr_xNiO_{4\pm\delta}$ solid solution have shown all compositions in the range $0 < x \leq 1.5$ to adopt the undistorted tetragonal K_2NiF_4 structure, describable in the $I4/mmm$ space group (1, 2, 16, 29). Recent laboratory X-ray powder diffraction data have been interpreted in terms of a monoclinic distortion beyond $x = 0.2$ (30).

The a and c lattice parameters for members of the $La_{2-x}Sr_xNiO_{4\pm\delta}$ series with $0 \leq x \leq 1.0$ show a sharp minimum and maximum, respectively, in the region $x \approx 0.5$ (16) resulting in a maximum in the c/a ratio at this composition also ($(c/a)_{max} = 3.345$). The initial interpretation of the unusual increase in a beyond $x = 0.5$ and associated maximum in the c/a ratio was that Ni^{III} was in the low-spin state and initially ($x < 0.5$) adopted the orbital ordering $t_{2g}^6\ (z^2)^1$. Increased oxidation beyond $x = 0.5$ was suggested to produce a configuration change to $t_{2g}^6\ (x^2-y^2)^1$ which both increases the in-plane bond length and enhances the conductivity due to the increased mobility of the holes in the x^2-y^2 orbital (16). Subsequent X-ray Rietveld refinements found no evidence for an anomaly in the $Ni-O_{ax}$ distance (which decreased linearly with x) or $Ni-O_{eq}/Ni-O_{ax}$ ratio at the composition corresponding to the maximum in c/a (which occurred at $x = 0.6$ in this study), and the anomaly in c/a was associated with the variation in the distance between the A cation and the axial oxygen in the rock-salt layer (1).

To date, our knowledge of the variation of the structure with nickel oxidation state has been limited to powder X-ray diffraction studies. Since changes in the electronic structure of the nickel cations are expected primarily to influence the Ni–O bond lengths, we have undertaken a systematic study using powder neutron diffraction in the concentration region where there has been controversy over the interpretation of the variations in the a and c lattice parameters and their consequences for the electronic structure and orbital ordering at the nickel center. In the course of the study, we have had to investigate a variety of synthesis routes to the $x = 1.0$ composition in order to prepare samples refineable using single phase models on high resolution diffraction data. It appears that the synthesis temperatures routinely used in the literature are insufficient to yield single phase material in the large x region (although they are satisfactory for $x < 0.9$).

EXPERIMENTAL

The citrate sol-gel technique was employed to synthesise polycrystalline 5 g samples of $La_{2-x}Sr_xNiO_{4+\delta}$ ($x = 0.4$, 0.5, 0.6, 0.8, 0.9, and 1.0). Stoichiometric quantities of La_2O_3 (99.999%, Aldrich), predried in air at 800°C to remove adsorbed water and carbon dioxide, $SrCO_3$ (99.994%, Alfa), and Ni powder (99.999%, Aldrich), as appropriate, were dissolved in a minimum quantity, typically 150 mL, of a 1 : 1 solution of analar 6 M nitric acid and distilled water. Then, 5 mL of analar ethylene glycol (99.5%, BDH) and one equivalent of citric acid per mole of M^{3+} cation (99.5%, BDH) were added and the solution heated at 150°C on a hot

plate with constant stirring for approximately 3 hours. The pale green gel thus formed was decomposed by further heating at 300°C for approximately 24 hours. The resulting fine brown powder was ground, returned to the furnace in air at 800°C for between 24 and 48 hours, then pressed into 13 mm diameter 1 g pellets at 5 tons. The pellets were annealed in a tube furnace at 1250°C in 1 atmosphere of flowing oxygen (BOC gases) for 6–8 days with several intermittent grindings. The products were allowed to cool to room temperature under the oxygen flow at the rate of the furnace, typically 12 hours, before being removed.

To investigate the effect of oxygen content (δ), as well as dopant concentration, upon the structure of $LaSrNiO_4$, samples were subsequently subjected to low temperature oxygen annealing at 1 atmosphere (500°C for 2 days) and 285 atmospheres (400°C for 6 hours) and to higher temperature oxygen annealing at 1 atmosphere (1450°C for 4 days). The oxygen pressure was generated by a Fluitron diaphragm compressor and the sample contained in gold foil in a home-built Rene41 cold-seal vessel. In view of the results of high resolution powder neutron diffraction measurements upon the samples thus prepared, subsequent syntheses of 3 g $La_{2-x}Sr_xNiO_{4+\delta}$ samples with $x = 0.2$, 0.33, and 0.4 were carried out as described above, but with a final firing temperature of 1450°C, rather than 1250°C. The temperature of the tube furnace containing the samples was ramped from 1000 to 1450°C at a rate of $5^\circ\,min^{-1}$, held at 1450°C for 50 hours and then ramped down to room temperature at the same rate. The samples were then ground, repelletized and the process repeated such that the total firing time at 1450°C was 100 hours. The progress of all the reactions described were monitored by powder X-ray diffraction, using a Philips automated PW 1710 diffractometer with Cu$K\alpha$ radiation over the 2θ range 5 to 70°, with a scan speed of $0.05^\circ\ 2\theta\ s^{-1}$.

High resolution powder neutron diffraction data were collected for samples with $x \geq 0.4$ (prepared at 1250°C) at 5 and 298 K on the time-of-flight (TOF) diffractometer HRPD at the ISIS spallation source, Rutherford Appleton Laboratories (RAL). Measurements were taken at the 1 m sample position over the TOF range 30,000–130,000 μs (corresponding to a d-spacing range of 0.6–2.6 Å) with a $\Delta d/d$ resolution of 8×10^{-4}. For data collected at 5 K the sample was contained in an ILL "orange" cryostat. The raw data were normalized to the incident beam and calibrated for detector efficiency by dividing by a standard vanadium run collected under the same conditions prior to refinement.

For samples with $x = 0.2$, 0.33, and 0.4, prepared at 1450°C, constant wavelength powder neutron diffraction data were collected at 15, 90, 150, and 298 K using the multidetector BT1 diffractometer ($\Delta d/d = 2 \times 10^{-3}$) at the National Institute of Standards and Technology (NIST), Gaithersburg, MD at a neutron wavelength of 1.5396 Å. Individual data sets were corrected for zero-point error and detector efficiency before being merged into a single profile between 12 and 142°. The samples were mounted in vanadium cans and cooled in a closed-cycle helium refrigerator.

Crystal structure analysis was performed by the Rietveld method (31). Data collected at RAL were refined using programs in the Cambridge Crystallographic Subroutines Library (CCSL) (31–34). The TF12LS (time of flight least squares) program, incorporating a four term Voigt peak shape convoluted with double exponential decay and switch function and a 15 term Chebyshev polynomial background function, was initially employed to refine the data collected for all compositions. Subsequently refinement of the data collected for the $x = 1.0$ sample, annealed at 1450°C under 1 atmosphere of flowing O_2, was carried out using the SAPS (structure and peak shape) refinement program which incorporates the same polynomial background and Voigt peak shape functions as TF12LS, but allows the refinement of *hkl* dependent anisotropic line-broadening across the pattern, by assigning individual Gaussian and Lorentzian peak shape parameters to each reflection (35). For the samples measured at NIST, profile refinements were performed using the GSAS program suite (36), incorporating a 10 term cosine Fourier background function and a five term pseudo-Voigt peak shape function.

The Ni^{III} content of the samples prepared was determined by iodometric titration against a standardized potassium thiosulphate solution. For each composition the titration was repeated a minimum of three times, until concordant results were obtained. Thermogravimetric analysis was also carried out, using a Rheometric Scientific STA 1500 thermal analyzer. Samples weighing approximately 50 mg contained in platinum crucibles were placed in the apparatus which was then purged for at least 30 minutes with H_2, predried over activated molecular sieves. Samples were subsequently heated to 800°C at a rate of $5^\circ\,min^{-1}\,in^{-1}$ under the gas flow.

RESULTS

The purity of the samples prepared was confirmed by laboratory powder X-ray diffraction measurements which revealed no impurities or starting materials. All members were found to crystallize in the tetragonal K_2NiF_4 structure in the $I4/mmm$ space group.

Oxygen Content Analysis

The results of the iodometric titrations and thermogravimetric analyses (TGA) are given in Table 1.

Powder Neutron Diffraction

The crystal structures, at 298 and 5 K, of the $La_{2-x}Sr_xNiO_{4+\delta}$ samples prepared at 1250°C under 1

TABLE 1
Oxygen Content (δ) and Average Nickel Oxidation State of $La_{2-x}Sr_xNiO_{4+\delta}$ Determined by Iodometric Titration and Thermogravimetric Analysis (TGA)

		Oxygen content (δ)			Ni Oxidation state	
x	Final synthesis conditions	Iodometry	TGA	Average	$\delta = 0$	Actual
0.2	1450°C, 1 atm. O_2	0.04(2)	0.07(1)	0.055	+ 2.20	+ 2.31
0.33	1450°C, 1 atm. O_2	0.02(2)	0.06(1)	0.040	+ 2.33	+ 2.41
0.4	1450°C, 1 atm. O_2	0.01(2)	0.06(1)	0.035	+ 2.40	+ 2.47
0.4	1250°C, 1 atm. O_2	0.02(2)	0.04(1)	0.030	+ 2.40	+ 2.46
0.5	1250°C, 1 atm. O_2	−0.01(2)	0.03(1)	0.010	+ 2.50	+ 2.52
0.6	1250°C, 1 atm. O_2	−0.03(2)	0.01(1)	−0.010	+ 2.60	+ 2.58
0.8	1250°C, 1 atm. O_2	−0.01(2)	0.00(1)	−0.050	+ 2.80	+ 2.70
0.9	1250°C, 1 atm. O_2	−0.01(2)	0.00(1)	−0.050	+ 2.90	+ 2.80
1.0	1250°C, 1 atm. O_2	−0.08(2)	−0.01(1)	−0.045	+ 3.00	+ 2.91
1.0	1450°C, 1 atm. O_2	—	−0.02(1)	—	+ 3.00	+ 2.96
1.0	500°C, 1 atm. O_2	—	0.00(1)	—	+ 3.00	+ 3.00
1.0	400°C, 285 atm. O_2	—	0.02(1)	—	+ 3.00	+ 3.04

Note. The final temperature and gaseous atmosphere used in the synthesis of each composition are given, for details of previous thermal treatments see main text.

atmosphere of flowing O_2 ($x = 0.4$, 0.5, 0.6, and 1.0, measured on HRPD) and 1450°C ($x = 0.2$, 0.33, 0.4 measured at NIST), were initially refined in the tetragonal $I4/mmm$ space group. The positional and thermal parameters obtained are available as supplementary material. The unit cell parameters and volumes and A–O and Ni–O bond lengths and derived bond valence sums at 298 K are present in Table 2. Anisotropic temperature factors were refined for the oxide anions. Refinement of the oxygen fractions corresponded within error limits to 4.00 oxygen per formula unit, and thus the occupancies were fixed in the final refinements. The refined parameters for the $x = 0.4$ phases prepared at 1250°C (HRPD) and 1450°C (NIST) were very similar.

Small NiO impurity peaks were observed in some of the data sets, the fraction reaching a maximum value of 6 mole% in the $x = 1.0$ prepared at 1250°C. Inclusion of NiO as a second minority phase in the refinements made no significant improvement to the fit and so no attempt was made to model or exclude the impurity peaks in the final analyses.

No superstructure reflections indicative of a larger cell were observed in any of the data sets and thus refinements in the lower symmetry space groups reported for other K_2NiF_4 structure transition metal oxides ($Pccn$, $P4_2/ncm$, Bmab) (19) proved to be unstable for both the 5 K and room temperature data sets. In the case of the 5 K data set for the $x = 0.4$ sample measured on HRPD, refinement in the $Fmmm$ orthorhombic space group resulted in a small reduction of χ^2 from 2.73 to 2.67, while that in $Cmca$ led to an extremely similar fit to that obtained in $Fmmm$. In light of

TABLE 2
Bond Lengths (Å) for $La_{2-x}Sr_xNiO_{4+\delta}$ Obtained from Rietveld Refinement of Powder Neutron Diffraction Data, Collected at 298 K at RAL ($x = 0.4-1.0$) and NIST (0.2, 0.33)

	0.2	0.33	0.4	0.5	0.6	0.8	0.9	1.0
Ni–O(1) × 2	2.201(3)	2.209(2)	2.207(2)	2.202(2)	2.177(2)	2.121(3)	2.095(4)	2.049(3)
Ni–O(2) × 4	1.9207	1.9134	1.9095	1.9059	1.9038	1.9072	1.9101	1.9120
La/Sr-O(1) × 1	2.391(3)	2.389(3)	2.400(2)	2.405(2)	2.414(2)	2.419(3)	2.423(5)	2.452(3)
La/Sr–O(1) × 4	2.7521(5)	2.7432(4)	2.737(1)	2.730(1)	2.724(1)	2.724(1)	2.727(1)	2.727(1)
La/Sr–O(2) × 4	2.604(1)	2.599(1)	2.596(1)	2.596(1)	2.597(1)	2.581(1)	2.573(2)	2.570(1)
c/Å	12.7008(3)	12.7086(2)	12.73045(2)	12.74029(2)	12.71352(5)	12.5597(1)	12.4822(1)	12.42830(2)
c/a	3.3063(1)	3.3209(1)	3.33345(1)	3.34297(1)	3.33896(2)	3.29273(4)	3.26737(5)	3.24984(1)
V/Å^3	187.413(7)	186.116(5)	185.67	185.04	184.32	182.74	182.17	181.77
Ni bond valence sum (298K)	2.40	2.43	2.46	2.48	2.52	2.59	2.61	2.67
Ni oxidation state	2.31	2.41	2.47	2.52	2.58	2.70	2.8	2.96

Note. The errors in the Ni–O(2) bond length are in the fifth decimal place and not quoted. The a lattice parameter is exactly twice the Ni–O(2) bond length.

the recent report of $F112/m$ symmetry beyond $x = 0.2$, refinement in this space group was attempted for all data sets. For $x < 0.6$, the refinements converged with γ within experimental error of 90° but no improvement to the fit was obtained, even for the $Fmmm$ $x = 0.4$ sample at 5 K. For $x > 0.6$, the monoclinic refinements were unstable.

The oxygen concentrations determined by titration and TGA indicate that interstitial oxygen defects were incorporated into the structure for $x \leq 0.4$. Attempts to place such interstitial oxygen atoms, O(3), near the (1/4, 1/4, 1/4) site previously reported for $La_2NiO_{4\pm\delta}$ (37) proved unstable, resulting in exceedingly large values of the isotropic temperature factor for the additional site. The extent of excess oxygen incorporation in the samples studied here is much less than found $La_2NiO_{4+\delta}$, where $\delta \approx 0.25$, and this prevents the refinement of the interstitial oxygen defects.

The diffraction data for $LaSrNiO_4$ ($x = 1.0$) prepared at 1250°C did not refine satisfactorily in $I4/mmm$, with a χ^2 value of 22.6. Inspection of the profile showed that this was due to poor fitting of the peak shape over the entire TOF range. Numerous peaks displayed extra features or shoulders, but no systematic hkl dependence of these abnormalities could be found, so it proved impossible to refine a separate peak shape for these reflections. Attempts to refine the data in alternative space groups proved both inferior and unstable. To ensure that this observation was not an anomaly, data were collected at 298 K on another $LaSrNiO_{4+\delta}$ sample, which had been prepared in an identical manner, and found to exhibit exactly the same features.

Multiple phase refinements of the $x = 1.0$ sample prepared at 1250°C were then carried out using the GSAS refinement package. Attempts to incorporate more than three $I4/mmm$ phases into the model were unsuccessful, while refinement with two phases did not result in satisfactory agreement. The final refinements were therefore performed with a three-phase model. The lattice parameters, phase fractions, and atomic positions plus anisotropic displacement ellipsoids (constrained to be equal for equivalent atoms in the different phases) for each phase were successfully refined. Refinement of the oxygen content for the three phases led to values, which, when combined with the appropriate mole fractions, gave a calculated overall stoichiometry of $LaSrNiO_{3.25}$, clearly inconsistent with that obtained by iodometry of $LaSrNiO_{3.955}$, so the oxygen occupancies were fixed in agreement with the iodometry results. The number of phases present and their unconventional peak shapes produce significant correlations between lattice, profile, and phase fraction parameters. This parameter correlation between the component phases and their pronounced sensitivity to the description of the thermal motion and site occupancies required the introduction of chemically sensible constraints. The c/a ratio is approximately linear in x over the $0.6 \leq x \leq 1.0$ region (Fig. 1), which allows us to associate the phases in the refinement model

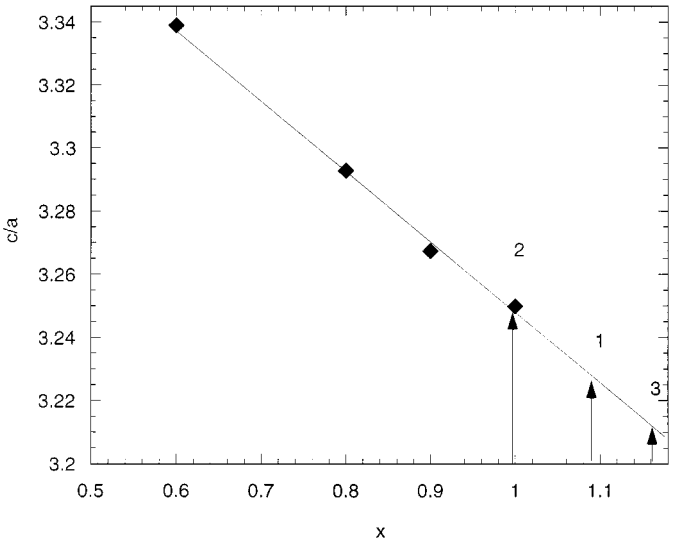

FIG. 1. Linear fit to a plot of c/a versus x at 298 K for $La_{2-x}Sr_xNiO_{4+\delta}$ samples with $0.6 < x < 1.0$. The c/a ratios for the three constituent phases in the multiphase refinement of powder neutron data for $LaSrNiO_{3.955}$ are marked with arrows.

with different La/Sr ratios through the x value obtained from the observed c/a, as shown in Fig. 1. The significant and robust feature of all refined models is the presence of a majority (70–76%) phase with a c/a ratio consistent with $x = 0.99$ in $La_{2-x}Sr_xNiO_4$. Refinement was always significantly improved by describing the Lorentzian strain broadening of this phase anisotropically using the empirical tensor formulation of von Dreele (36). The lattice parameters of the two minority phases, and thus the assigned value of x, are strongly correlated with the peakshape description applied and the existence of strain-induced displacements of the Bragg peak positions in all the phases, as these phases display enhanced Gaussian and Lorentzian broadening compared with the majority phase. A three-phase model without strain-induced Bragg peak displacement refines to $\chi^2 = 7.0$, while introduction of the anisotropic strain displacement (parameterized as $d = d_0 - \varepsilon_a d \cos\phi$ where ϕ is the angle between the scattering vector and the [001] direction; i.e., the displacement is most pronounced for Bragg peaks with large values of l) for all phases reduces χ^2 to 5.3, with $x = 1.06$ (and a phase fraction of 8.0(3) mole%), 0.99 (71(3)%), and 1.04 (21(1)%). This anisotropic peak displacement is an order of magnitude larger for the minority phases, consistent with the similar enhancement in Gaussian (phase 3) or Lorentzian (phase 1) broadening parameter deriving from strain, i.e., a constant $\Delta d/d$ width deriving from the distribution of lattice parameters $\Delta a/a$ and $\Delta c/c$. The physical meaning of assigning x values to the phases from their c/a ratios is demonstrated because the mean composition of the sample can be

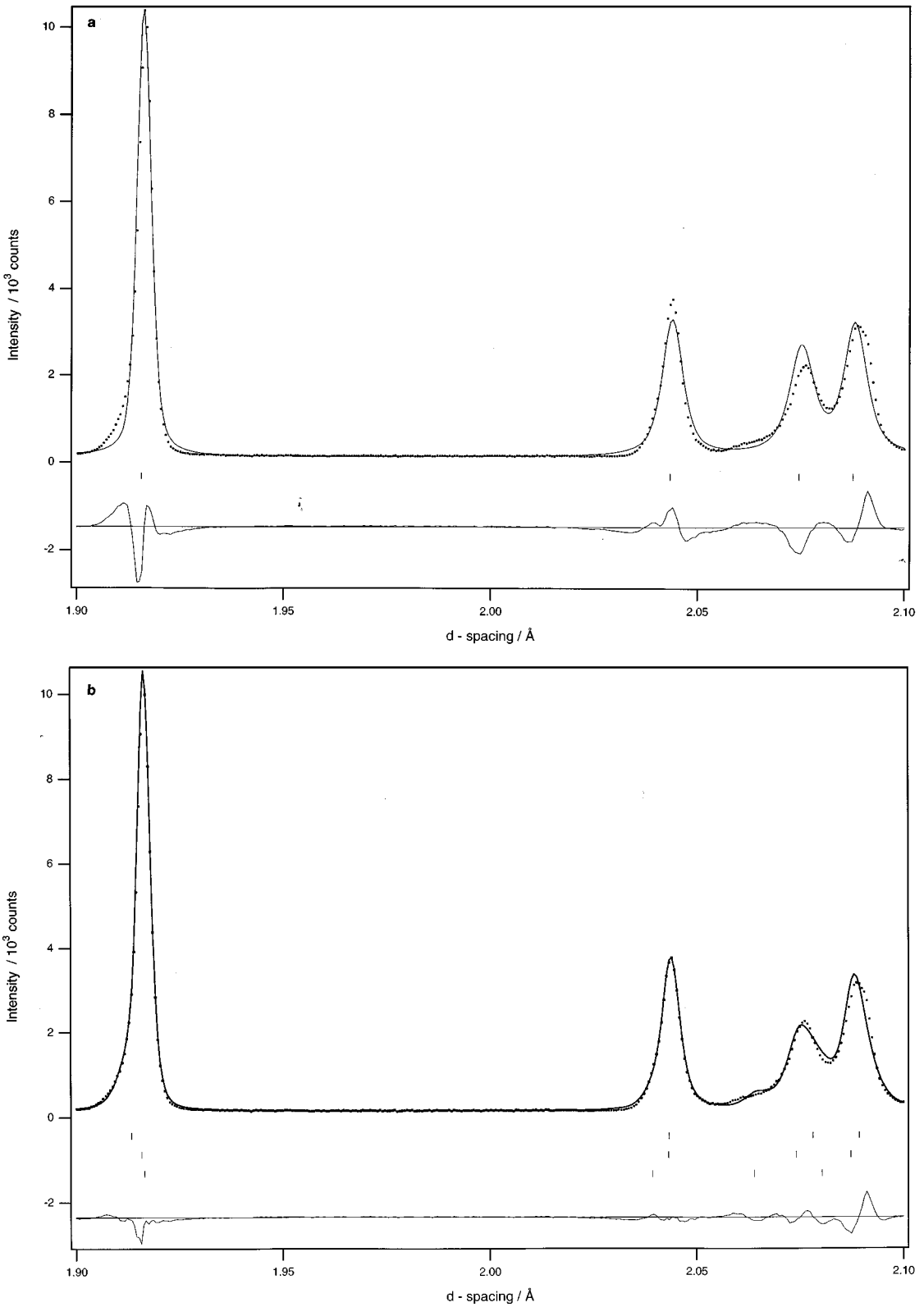

FIG. 2. 1.9–2.1 Å region of the TOF neutron diffraction pattern of $LaSrNiO_{3.955}$ prepared at 1250°C. Rietveld refinement with (a) single phase model and (b) three phases with anisotropic broadening for the majority phase. (c) As in (b) but with anisotropic strain-induced peak displacement in each phase, adopted as the final model. Observed (markers), calculated (line), and difference profiles are shown. The indices of the Bragg reflections in this region are shown in Fig. 4.

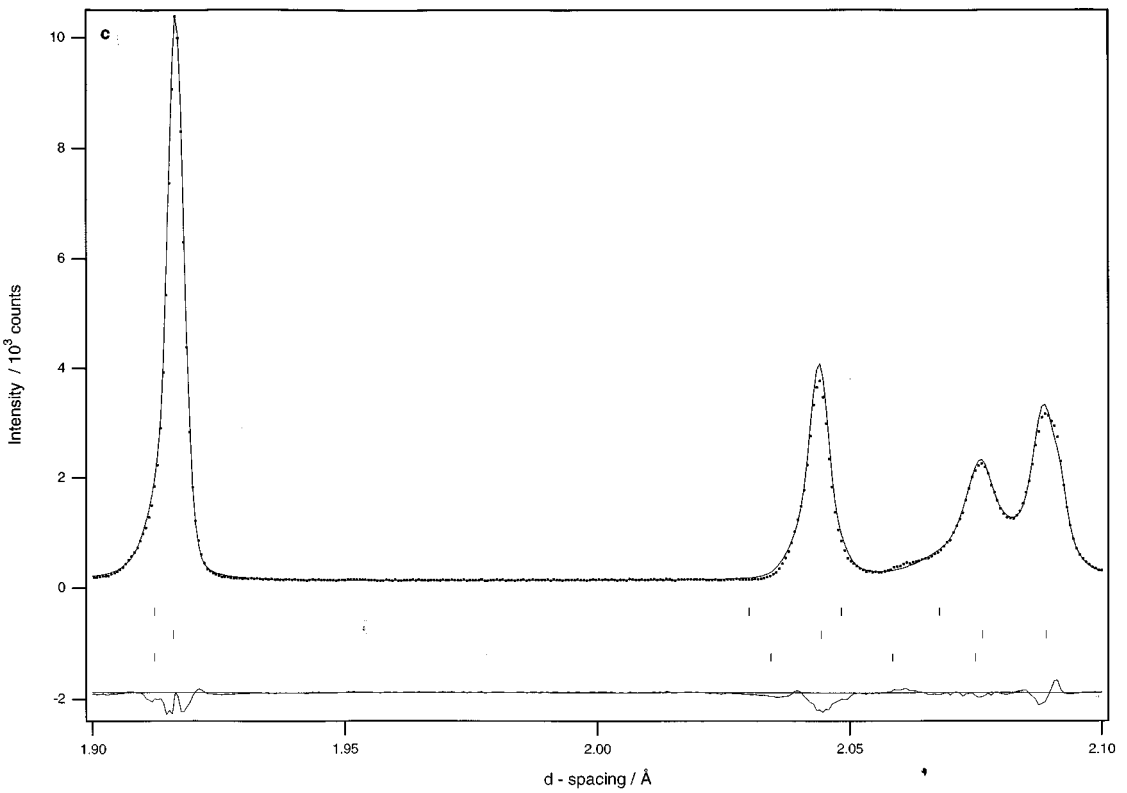

FIG. 2—*Continued.*

computed from the phase fractions and assigned x values as $La_{0.99}Sr_{1.01}NiO_4$. The introduction of anisotropic strain broadening for the most predominant minority phase led to a final χ^2 value of 4.4. The Gaussian broadening parameters for the majority and most abundant minority phase were constrained to be equal, while the broadening of the least abundant minority phase was almost exclusively Gaussian and considerably larger than that for the other two phases. Refinement stability required that the a parameters of the two minority phases were constrained to be equal—this is chemically sensible in view of their similar x values and the much more pronounced dependence of c on La/Sr ratio noted for smaller values of x. This model is adopted not only on the grounds of agreement indices: the $1.9 \leq d/\text{Å} \leq 2.10$ region is extremely poorly fitted in the single phase refinement and thus very sensitive to the multiphasic and strained nature of the sample. Figure 2 shows the fit to this region in refinement models containing a single phase, three phases without peak displacement and three phases with peak displacement and minority phase anisotropic broadening. The significant improvement in the fit to this region of the pattern leads us to adopt the complex final model for which the full profile refinement is given in Fig. 3. This improved description of the peakshape changes the c/a values and derived x values significantly, to $x = 1.09$ (14.9(6)%), $x = 0.99$ (76(3)%), and $x = 1.16$ (9.1(5)%). The La/Sr ratios in each phase were fixed at the values derived from c/a. The mean composition derived from the c/a ratios and phase fractions is $La_{0.99}Sr_{1.01}NiO_4$. The refined cell and peakshape parameters for each phase are quoted in Table 3 together with the bond lengths in the majority phase. A significant reduction in χ^2 arose from allowing the U_{33} component of the anisotropic displacement tensor of the axial oxygen in the $x = 1.16$ phase to take a different, larger value than for this atom in the other two phases. This indicates either enhanced disorder in this phase or the existence of an excess of oxygen vacancies in this phase over the 1.5% deficiency from full occupancy assigned to all the phases on the basis of TGA results.

In order to investigate the cause of this phase segregation at large x values under conventional literature synthesis conditions more thoroughly, as a function of oxygen content (δ), as well as dopant concentration (x), data were collected on $La_{2-x}Sr_xNiO_{4+\delta}$ samples with $x = 0.8, 0.9, 1.0$ prepared initially as before, but then subjected to low, 500°C, and high, 1450°C, temperature, annealing under 1 atmosphere flowing O_2 ($x = 1.0$) and to high oxygen pressures, 285 atmospheres at 400°C ($x = 0.9$ and 1.0). All

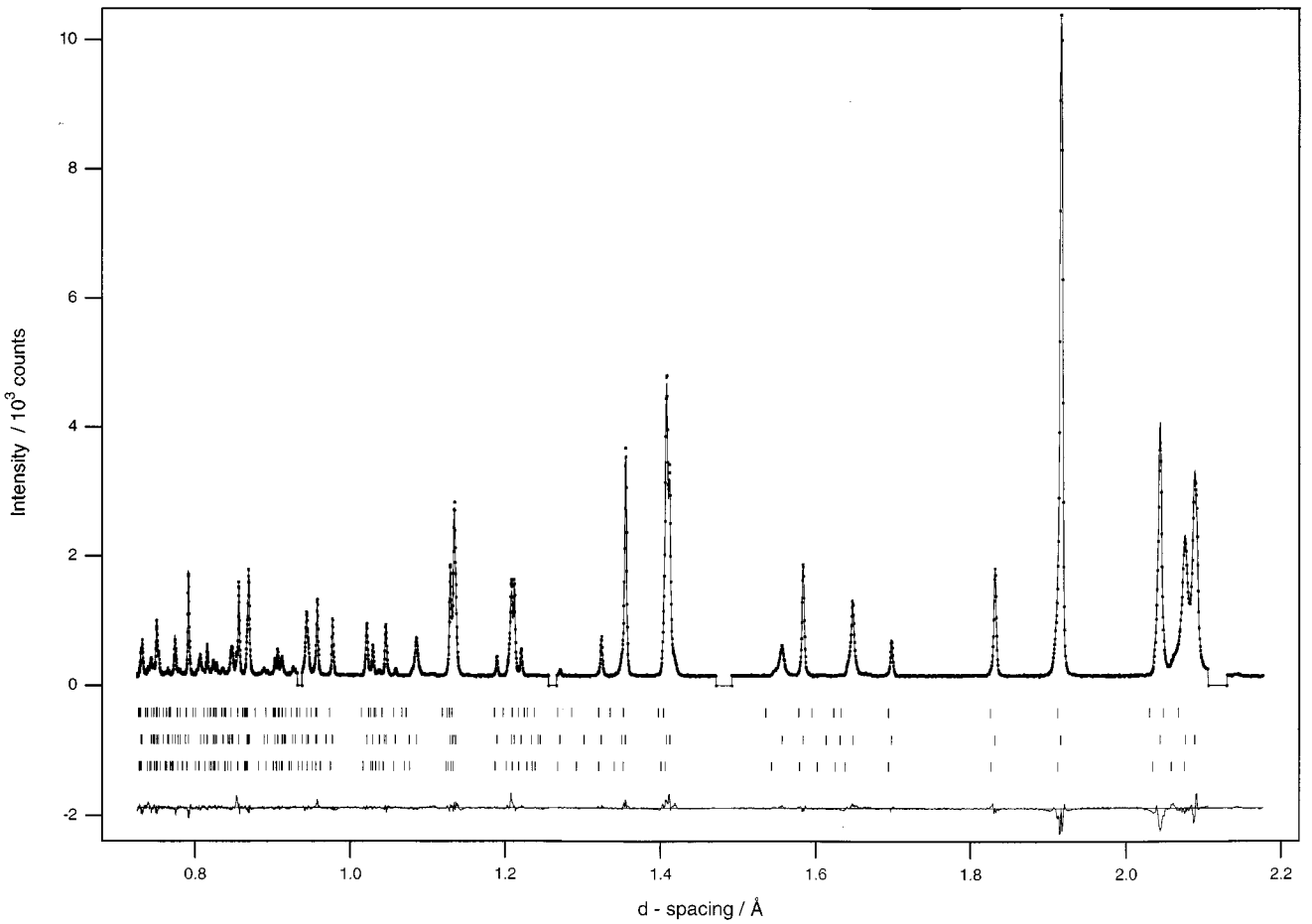

FIG. 3. Observed (markers), calculated (line), and difference profiles for the three phase refinement of room temperature powder neutron data for $LaSrNiO_{3.955}$ according to the model shown in Fig. 2c. The tick marks correspond to phase 3 (top), phase 2 (middle), and phase 1 (bottom), respectively.

data were collected on the HRPD diffractometer over the TOF range 30,000–130,000 μs at 298 K. Inspection of the data collected for the $x = 0.8$ and 0.9 samples does reveal the same unusual peak shape features found for the $x = 1.0$ compound but to a much lesser degree. Hence, the data for these samples were refined satisfactorily in the tetragonal $I4/mmm$ space group as described previously for samples with $x \leq 0.6$.

Focusing on $LaSrNiO_{4+\delta}$, the multiphasic nature described above for samples prepared at 1250°C is enhanced for those samples which have been annealed at low temperatures, both under ambient and high pressures of oxygen, whereas the sample annealed at 1450°C shows the sharpest Bragg peaks, as can be seen in Fig. 4. Even so, successful fitting of the latter data required the use of the SAPS program, which allows the refinement of *hkl* dependent anisotropic line broadening across the pattern, by assigning individual peakshape parameters to each reflection; i.e., all the Bragg peaks are described by a single Voigt function but the width variation across the diffraction pattern is unconventional indicating possible strain, domain, or crystallite size effects. This approach is in contrast to the multiphase refinement analysis which is necessary when the observed peaks cannot be fitted to a single Voigt function regardless of width, but rather two, or more, functions are required to reproduce the observed profile. In the SAPS analysis, carried out over the TOF range 50,000–119,000 μs, the oxygen site occupancies were fixed to be the same as those for the standard universal peakshape refinement (TF12LS), and isotropic temperature factors were employed as it proved necessary to minimize number of variables involved. An enlargement of the fits obtained using TF12LS and SAPS over the TOF region 97,500–101,500 μs are shown in Figs. 5a and 5b. The structural parameters obtained from the two refinements are also listed in Table 4. Refinement in $F112/m$ yields $\chi^2 = 27.4$ with a much poorer fit.

The crystal structures at 150, 90, and 15 K of the $La_{2-x}Sr_xNiO_{4+\delta}$ samples with $x = 0.2$, 0.33, and 0.4

TABLE 3
Structural Parameters of $LaSrNiO_{3.955}$ Prepared at 1250°C obtained from a three phase Rietveld Refinement of Powder Neutron Diffraction Data Collected on HRPD at 298 K

Phase	1	2	3
Mole fraction (%)	14.9(6)	76(3)	9.1(5)
a/Å	3.8247(2)	3.83204(2)	3.8247(2)
c/Å	12.351(3)	12.4585(5)	12.290(6)
V/Å^3	180.67(6)	182.948(8)	179.8(1)
c/a	3.229	3.251	3.213
x derived from c/a	1.09	0.99	1.16

Note. The single phase model used for other members of the series refined to $\chi^2 = 22.6$.The refined positional and thermal parameters in the three phases are deposited as supplementary material. The anisotropic strain displacements of the Bragg peaks described in the text were 0.4, 0.06, and 1.35%, respectively for the three phases. The peak shapes for phases 1 and 2 were refined with identical Gaussian components ($\sigma^2 = \sigma_1^2 d^2 + \sigma_2^2 d^4$: $\sigma_1 = 1130(19)$ for both phases: $\sigma_2 = 650(60)$ for phase 2 only) and Lorentzian broadening $\gamma = \gamma_0 + \gamma_1 d$: $\gamma_0 = 13(1)$ for both phases; the strain broadening is given by $\gamma_1 = (h^2L_{11} + k^2L_{22} + l^2L_{33} + 2hkL_{12} + 2hlL_{13} + 2klL_{23})d^3$. $L_{11} = 7.4(5)$, 0.39(6); $L_{33} = 1.23(7)$, 0.82(1); $L_{13} = -3.12(1)$, $-0.72(2)$. The peak shape for the least abundant phase 3 was purely Gaussian with $\sigma_1 = 29020(5)$. The a and b lattice parameters of phases 1 and 2 were constrained to be equal. The Ni–O axial and equatorial bond lengths in the majority phase 2 are 2.047(2) Å and 1.91602(1) Å, respectively. $\chi^2 = 4.4$, $R_E = 2.65\%$.

(measured at NIST, and prepared at 1450°C under 1 atmosphere of flowing O_2) were refined successfully in the tetragonal $I4/mmm$ space group. Refinement of anisotropic temperature factors was significant only for the oxide anions. The positional and thermal parameters obtained and the corresponding bond lengths are available as supplementary material. The observed, calculated, and difference profiles for the refinement of $La_{1.67}Sr_{0.33}NiO_{4.04}$ at 298 K are shown in Fig. 6 and the structure of $La_{1.8}Sr_{0.2}NiO_{4.055}$ at 298 K showing the anisotropic thermal ellipsoids in Fig. 7. The evolution of the axial and equatorial bond lengths around nickel with temperature are presented in Fig. 8 together with the U_{ij} components of the axial oxygen displacement ellipsoid. The magnetic transition temperatures indicated by the onset of coherent oscillations in the μSR experiments are 133 K ($x = 0.2$), 204 K ($x = 0.33$—the charge ordering temperature at this composition is reported in the literature at 235 K), and 131 K ($x = 0.4$). Inspection of the temperature dependence of the refined structures indicates small changes in the NiO_6 octahedron on cooling which are not directly correlated with the onset of magnetic order. These are indicated by the variation in the ratio of axial to equatorial bond length with temperature in Fig. 8. The evolution of the axial and equatorial bond lengths at $x = 0.4$ is unremarkable (Fig. 8c). At $x = 0.33$, the Ni–O axial bond length increases by 0.005 Å on cooling from 150 to 90 K, together with an anomalous increase in the U_{33} component of the displacement ellipsoid of this anion (Fig. 8b plus inset). Further cooling to 15 K results in contraction, as expected. At $x = 0.2$, cooling from 298 to 150 K leads to an increase of 0.007 Å in the Ni–O axial

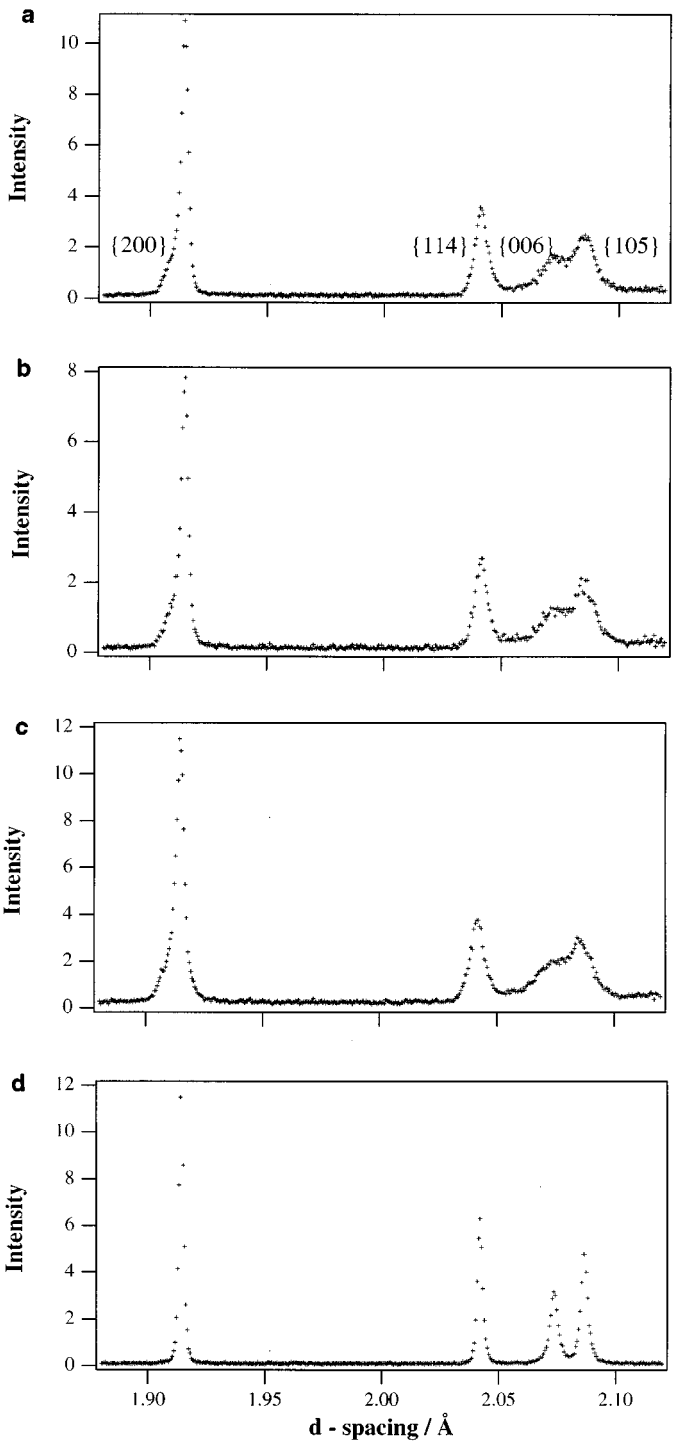

FIG. 4. Comparison of TOF powder neutron diffraction patterns, over 1.88–2.12 Å, for $LaSrNiO_{4\pm\delta}$ samples prepared at (a) 1250°C in 1 atmosphere O_2 and then annealed at (b) 500°C in 1 atmosphere O_2, (c) 400°C in 285 atmosphere O_2 and (d) 1450°C in 1 atmosphere of O_2.

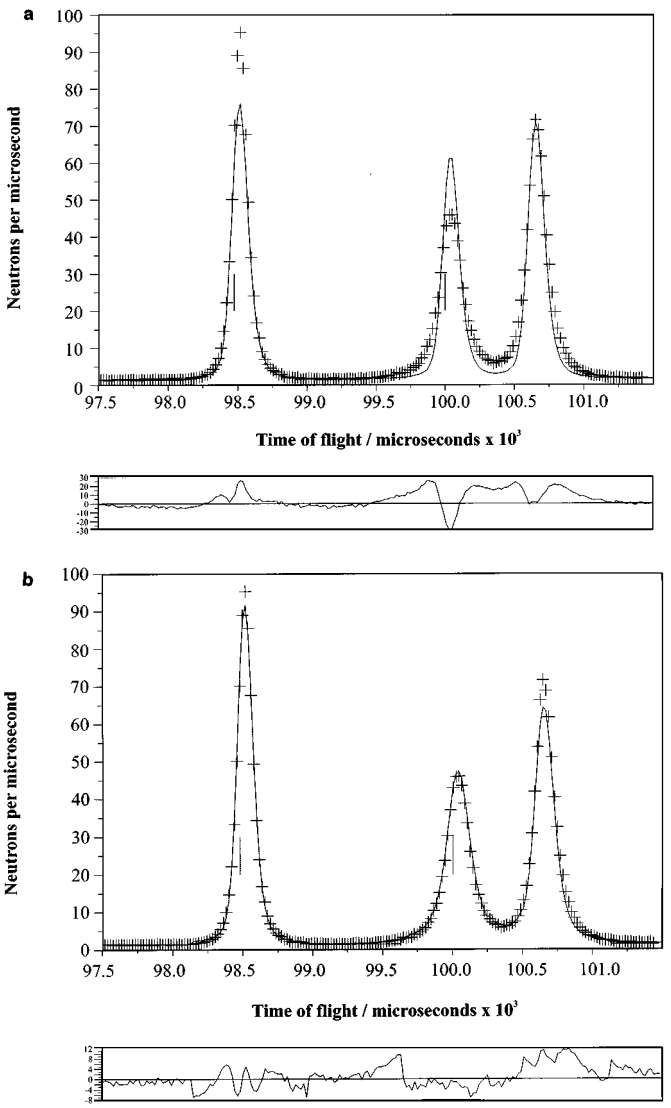

FIG. 5. Enlargement over the TOF region 97,500–101,500 μs of the Rietveld refinement of $LaSrNiO_4$, annealed at 1450°C in 1 atmosphere O_2, in the *I4/mmm* space group at 293 K using the (a) TF12LS (isotropic peak shape) and (b) SAPS (anisotropic peak width) programs. The difference plot is shown as the difference divided by the standard deviation of each point.

bond, also correlated with an anomalous increase in U_{33}: again both parameters resume conventional behavior on further cooling (Fig. 8a). These observations are significant only at the 1σ level but call for further detailed investigation into the evolution of the average structure of $La_{2-x}Sr_xNiO_4$ on cooling for $x < 0.4$.

DISCUSSION

Chemical Composition

The iodometry and thermogravimetric analysis results (Table 1) are consistent with those obtained by previous researchers (6, 16), illustrating that samples with low strontium contents tend to accommodate excess oxygen, while those with high strontium contents are slightly oxygen deficient. Naturally this is to be expected, as the greater the

TABLE 4
Structural Parameters of $LaSrNiO_{4+\delta}$ (prepared at 1450°C) Obtained from Rietveld Refinement of Powder Neutron Diffraction Data, Collected at 298 K at RAL in the *I4/mmm* Tetragonal Space Group

	x	1.0	
		TF12LS	SAPS
δ		−0.02	
a/Å		3.82407(1)	3.82428(1)
c/Å		12.42737(2)	12.42830(2)
V/Å^3		181.73	181.77
La/Sr	z	0.36195(9)	0.36163(8)
	B_{11}/B_{22} (Å^2)	0.63(2)	0.38(7)
	B_{33} (Å^2)	1.91(4)	0.38(7)
Ni	B_{11}/B_{22} (Å^2)	0.29(2)	0.25(8)
	B_{33} (Å^2)	2.16(6)	0.25(8)
O(1)	z	0.1647(1)	0.1639(1)
	B_{11}/B_{22} (Å^2)	1.03(4)	0.79(7)
	B_{33} (Å^2)	1.61(9)	0.79(7)
	Occupancy	0.947(8)	0.947
O(2)	B_{11} (Å^2)	0.88(6)	1.07(7)
	B_{22} (Å^2)	0.45(5)	1.07(7)
	B_{33} (Å^2)	2.66(8)	1.07(7)
	Occupancy	1.01(1)	1.01
	R_{wp} (%)	12.10	7.95
	R_e (%)	3.26	3.07
	R_I (%)	22.81	6.85
	χ^2	13.8	6.7

Note. The structural parameters obtained using a universal peak shape (TF12LS) and *hkl* dependent anisotropic line broadening (SAPS) are both given.

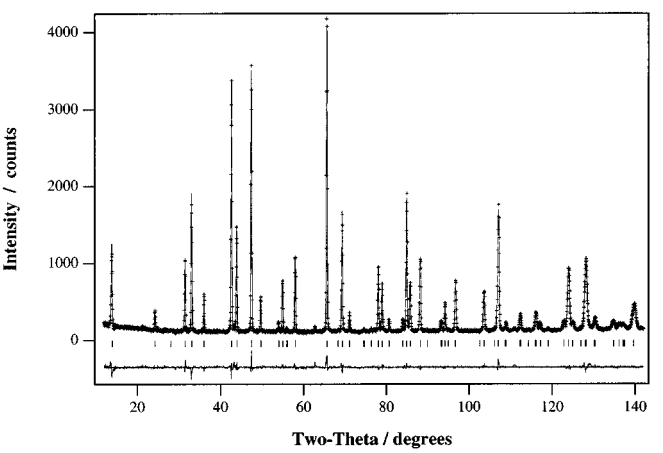

FIG. 6. Observed (markers), calculated (line), and difference profiles for the refinement of room temperature BT1 powder neutron data for $La_{1.67}Sr_{0.33}NiO_4$.

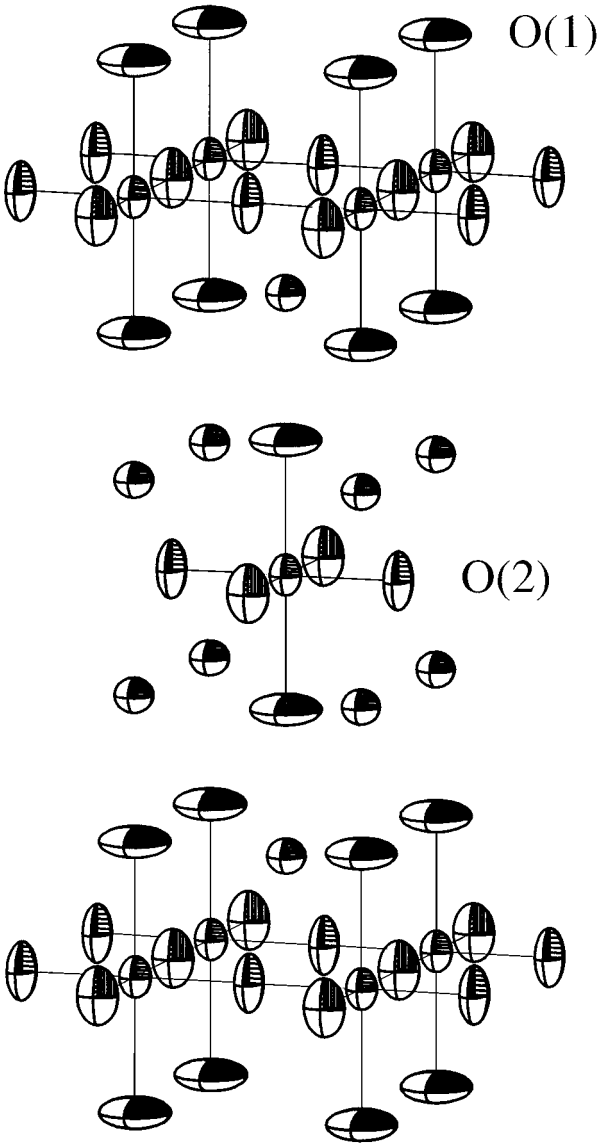

FIG. 7. ORTEP representation of the structure of $La_{1.8}Sr_{0.2}NiO_{4.055}$ at 298 K, determined by refinement of powder neutron diffraction data. The atoms are represented as 90% thermal ellipsoids.

value of x, the greater the proportion of Ni^{II} which must be oxidized to Ni^{III} in the sample in order to preserve overall charge neutrality if the oxygen stoichiometry is maintained. The extent of excess oxygen incorporation, even at low values of x, is much less than for $La_2NiO_{4+\delta}$, and as a result it is not possible to refine the location of the interstitial defects which must be formed from powder neutron diffraction data.

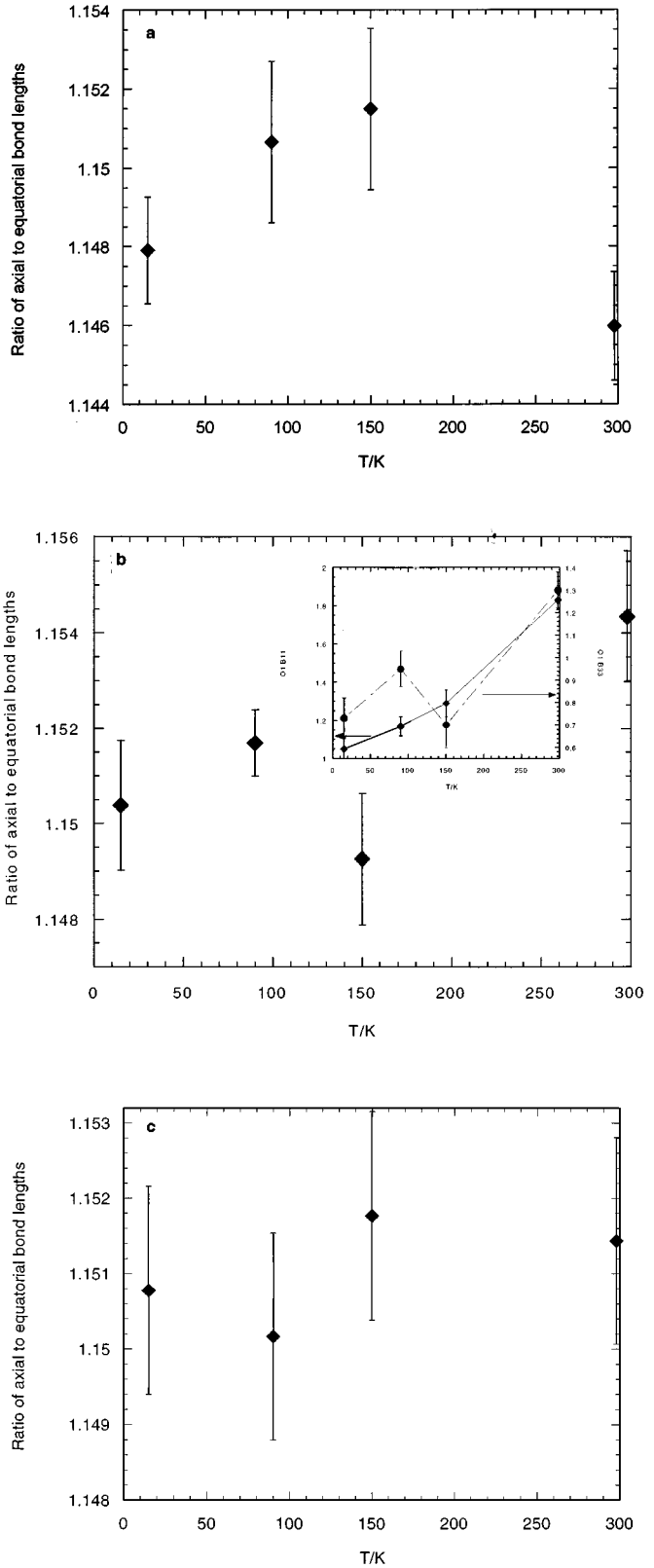

FIG. 8. The evolution of axial and equatorial bond lengths (Å) with temperature for $x = $ (a) 0.2, (b) 0.33, and (c) 0.4. The inset to (b) shows the evolution of U_{11} and U_{33} for $x = 0.33$.

Structural Evolution with x

The c/a values of 3.25–3.30 commonly found in K_2NiF_4 oxides are smaller than 3.414 ($c = (2 + \sqrt{2})a$) expected for a regular BO_6 octahedron and identical A–O bond lengths in the nine coordinate sites between the BO_2 layers (38). Compared to the ABO_3 perovskites, tilting of the octahedra due to reduction in the tolerance factor below 1.0 is less common, ascribed to the rigidity of the intervening rock-salt layers. Anisotropy in the BO_6 octahedron is ascribed to compression of the B–O(2) equatorial bond. The axial B-O(1) bond can lengthen as the charge on the A cation increases. Elongated BO_6 octahedra and short B–O(2)–B bonds are commonly found in many of the A_2BO_4 oxides. The extent of distortion depends on the electronic configuration and chemical identity of the B cation: the ratio of the B–O(2) axial to B–O(1) equatorial bond length is 1.27 for the Jahn–Teller distorted ^{2}E Cu^{II} cation in La_2CuO_4 while the almost equiaxial octahedra in $NdSrCrO_4$ have a ratio of 1.04 for the ^{4}A Cr^{III} cation (39). The distortion in $La_2NiO_{4.00}$ is much less pronounced than that in La_2CuO_4, with an axial/equatorial ratio of 1.15. However it is markedly more pronounced than in $NdSrCrO_4$, indicative of some difference in population of the x^2–y^2 and z^2 levels, in contrast to the $S = 1$ high spin ground state of Ni^{II} in regular octahedral coordination. This is consistent with the reduction in the observed staggered moment from 2 μ_B to 1.68(6) μ_B (19) and may be ascribed to some admixture in the solid of the low-spin state into the high-spin octahedral ground state of the isolated cation (1).

The variation of the a and c lattice parameters with x in the $La_{2-x}Sr_xNiO_{4+\delta}$ series is shown in Fig. 9a and the variation in c/a ratio with x in Fig. 9b. During this discussion data presented for the $x = 1.0$ composition at 298 K are from the SAPS refinement for the sample prepared at 1450°C under 1 atmosphere O_2 (Table 4) unless otherwise stated.

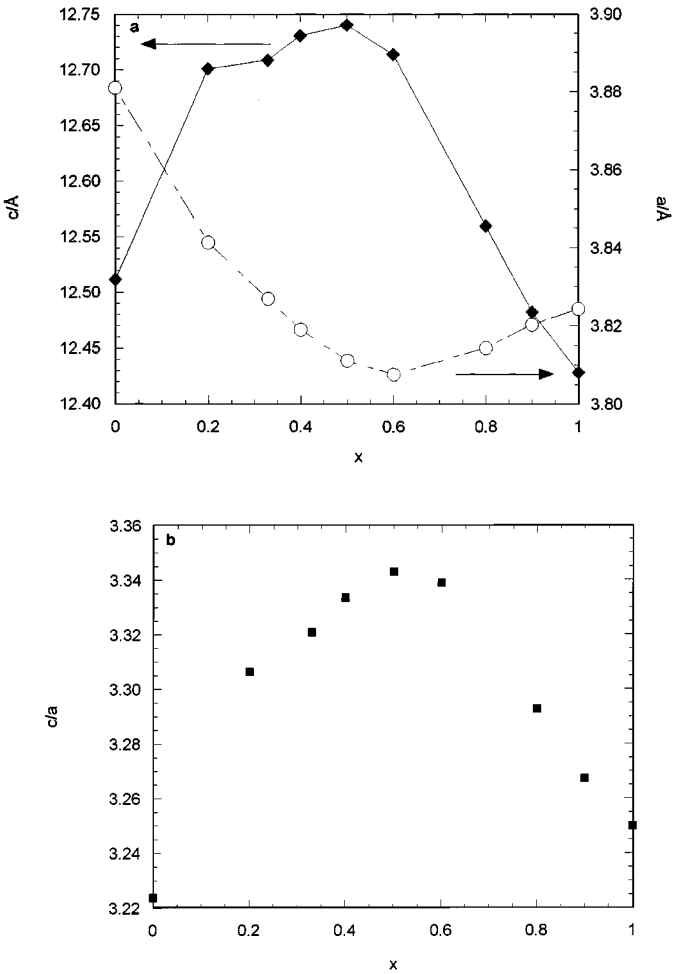

FIG. 9. (a) a (open circles) and c (filled diamonds) lattice parameters and (b) c/a ratio versus x at 298 K for $La_{2-x}Sr_xNiO_{4+\delta}$.

The observed lattice parameters are in qualitative agreement with those previously published (1, 2, 16, 18, 40); the a lattice parameter decreases up to $x = 0.6$ and increases thereafter while the c lattice parameter increases up to $x = 0.5$ and then decreases in the region $0.6 < x < 1.0$. This results in the tetragonality ratio c/a showing a maximum of 3.343 at the composition $x = 0.5$, in good agreement with the value of 3.345 reported by Gopalakrishnan *et al.* and others (Fig. 9) (16, 17). The unit cell volume shows a smooth virtually linear decrease with increasing Sr^{2+} concentration, x. The smaller ionic radius of the low-spin Ni^{3+} (0.56 Å) formed upon substitution compared to that of Ni^{2+} (0.70 Å) overcomes the increase in the A cation size from 1.22Å (La^{3+}) to 1.31 Å (Sr^{2+}) (41–43).

These trends in the lattice parameters have been explained in the literature in terms of a Jahn–Teller distortion due to orbital ordering in the low-spin $t_{2g}^6 e_g^1$ nickel(III) cation (16). The observation that a decreases while c increases up to $x = 0.5/0.6$ has been taken to indicate that this distortion produces four short (equatorial) and two long (axial) bonds and that the single e_g electron is initially ordered in the d_{z^2} orbital. As the c/a ratio in the K_2NiF_4 structure is normally found empirically to be around 3.30 at 298 K (16, 38, 44), except for when a Jahn–Teller distortion occurs, the distortion in $La_{2-x}Sr_xNiO_{4+\delta}$ must be weak as the c/a value is only slightly greater than this at its maximum value at $x = 0.5$. However, the value of c/a, and the extent of the distortion, then decreases quite dramatically as x increases to 1.0, $LaSrNiO_4$. Further increase in the amount of low spin Ni^{III} as x increases from 0.5 to 1.0 would be expected to produce more, rather than less, distorted octahedra if the electrons in the system remain localized.

The fundamental problem with these conclusions is that the trends in lattice parameters do not necessarily reflect variations in the Ni-O bond lengths across the series, and it is these that must be considered when discussing possible changes in electronic configuration at the nickel site, as pointed out by Takeda and co-workers (1). The fact that measurement of precise metal-oxygen bond lengths by powder X-ray diffraction is difficult has prevented conclusive resolution of this issue. Figures 10a and 10b show the variation of both the axial and equatorial Ni–O bond lengths versus x at 298 K.

The equatorial Ni–O(2) bond length decreases with increasing x up to $x = 0.6$ and then increases upon further Sr^{2+} substitution, while the axial Ni–O(1) bond length remains essentially constant in the composition range $0.2 \leq x \leq 0.5$, but then decreases markedly as x increases to 1.0. Note that the minimum in the equatorial bond length is at $x = 0.6$ while the decrease in the axial Ni-O distance is significant beyond $x = 0.5$. The ratio of these axial and equatorial Ni–O bond lengths is shown in Fig. 10c, and is found to be approximately constant for $0.2 \leq x \leq 0.5$ but then drops sharply, the NiO_6 octahedra being nearly equiaxial at $x = 1.0$. The fact that the variation in this ratio reflects changes in the axial Ni–O(1) bond length with composition indicates that the changes across the series in the axial bond are much greater than those observed for the equatorial Ni–O(2) bond. The Ni–O(1) bond decreases by $\sim 7\%$ between $x = 0.2$ and $x = 1.0$ while the Ni–O(2) bond length alters by only $\sim 1\%$ between $x = 0.2$ and $x = 0.6$. For $x = 0.0$–0.5 the percentage changes in both bonds are similar, resulting in only very minor changes in the distortion of the octahedron as measured by the ratio of the axial to the equatorial bond length or the mean square deviation of the bond lengths from the mean (in contrast with the results of previous X-ray Rietveld refinements (1)). When the variation is compared with that in the tetragonality ratio shown in Figure 9b, there are both similarities and differences in the trends observed. For $0.6 \leq x \leq 1.0$ the decrease in Ni–O(1)/Ni–O(2) mirrors that in the c/a ratio suggesting that variations in the coordination around the Ni site are responsible for the evolution of the lattice parameters in this region. However, the fact that the distortion of the NiO_6 octahedra changes little for $0.2 \leq x \leq 0.5$ while c/a increases indicates that the changes in the latter in this composition range are due to some other factor, such as the anisotropic expansion of the La/Sr–O rock-salt layer suggested previously (1).

The bond-valence sum around Ni in the samples is shown as a function of x in Fig. 11, along with the corresponding average Ni oxidation states. For most inorganic compounds the sum of the bond valences around any given atom lies within 0.1 of the formal oxidation state (45). As the formal oxidation state of the nickel ions in the samples under investigation is nonintegral, additional difficulties in

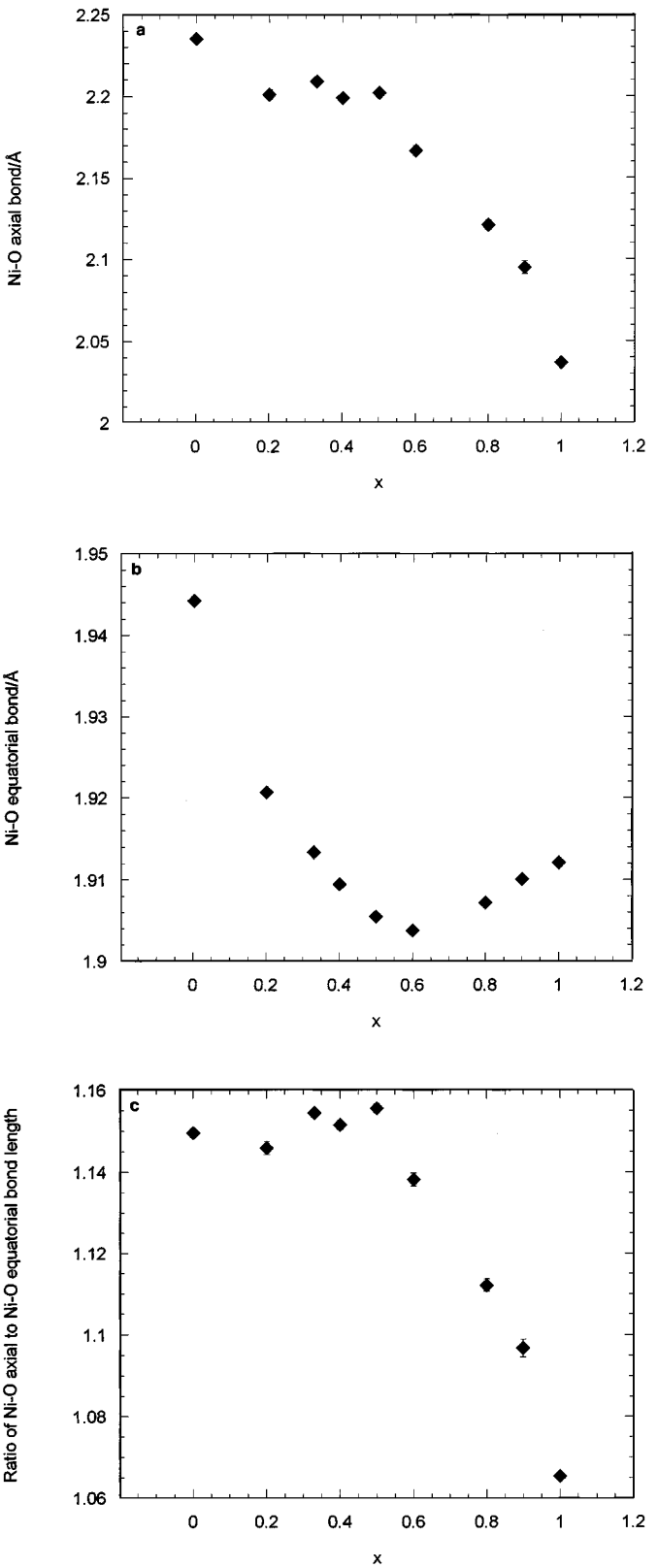

FIG. 10. (a) Axial and (b) equatorial Ni–O bond lengths in $La_{2-x}Sr_xNiO_{4+\delta}$ versus x at 298 K. (c) Ratio of the axial and equatorial Ni–O bond lengths versus x.

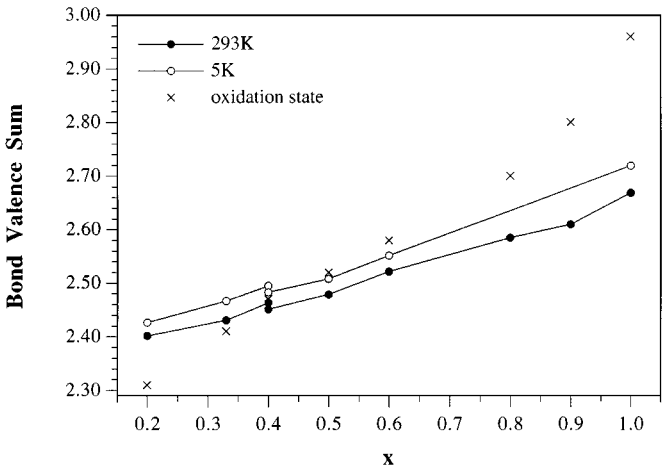

FIG. 11. Bond-valence sum around Ni in $La_{2-x}Sr_xNiO_{4+\delta}$ versus x at 298 and 5 K. The Ni oxidation state, determined from iodometric titration and thermogravimetric analysis, is included for comparison.

interpretation of the valences obtained have been introduced by employing the R_{ij} value determined for Ni^{II} in the calculations. However, previous work has shown that for many bonds to oxygen the bond-valence parameter is not strongly dependent upon oxidation state (e.g., Brown and Altermatt (46) obtained the following values of R_{ij} for bonds to oxygen from metal atoms in different oxidation states: Fe^{II} 1.73, Fe^{III} 1.76; Mn^{II} 1.79, Mn^{III} 1.76, Mn^{IV} 1.75). In fact, the value of R_{ij} for low-spin Ni^{III}–O calculated from $HoNiO_3$, (47) low-spin $AgNiO_2$ (48) and $LaSrNiO_4$ (49) is 1.68 Å, compared with 1.654 Å for Ni^{II}–O (50).

The bond-valence sum around Ni (Table 2) increases linearly with x over the composition range studied, as expected. For $0.33 \leq x \leq 0.6$ the calculated valences are in good agreement with the formal oxidation states calculated from iodometry and thermogravimetric analysis. At $x = 0.2$ the bond-valence exceeds the measured oxidation state but only by 0.092, which is less than the expected variation of 0.1; so for this composition also, the two values concur within error. For higher strontium concentrations than 0.6 the sums appear to systematically underestimate the formal valence, the degree of discrepancy increasing with x.

To fully interpret the changes in lattice parameters, c/a ratio, and Ni–O bond lengths with increasing strontium concentration, the changes in A cation coordination geometry must also be considered. Figures 12a–12c show the variation in La/Sr–O bond lengths with x at 5 and 298 K. The four La/Sr–O(1) bonds within the rock-salt layer decrease in length for $0.2 \leq x \leq 0.6$ and then remain constant within error, while in contrast the four La/Sr–O(2) bonds remain fairly constant in length for $0.2 \leq x \leq 0.6$, decreasing only slightly, before contracting as x increases to 1.0. The unique La/Sr–O(1) bond along the c axis, which as the shortest La/Sr–O bond will be most sensitive to the average A cation size and charge, becomes progressively longer as the alkaline earth concentration increases. This reflects the larger size and reduced charge of the Sr^{2+} cation. As discussed previously, due to competition between the A and

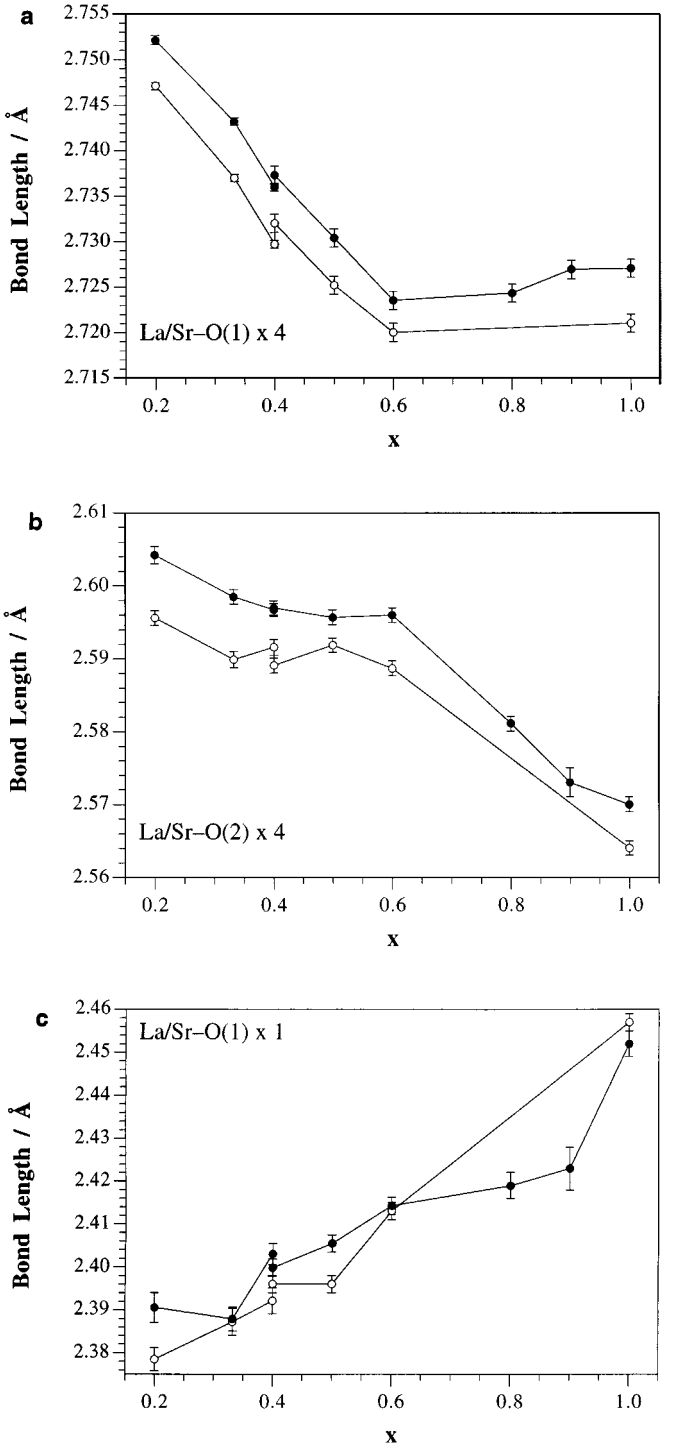

FIG. 12. La/Sr–O bond lengths in $La_{2-x}Sr_xNiO_{4+\delta}$ versus x at 298 K (filled circles) and 5 K (open circles); (a) La/Sr–O(1) × 4, (b) La/Sr–O(2) × 4, and (c) La/Sr–O(1) × 1.

B cations for bonding with the O(1) anions in the K_2NiF_4 structure, the average length of the unique La/Sr–O bond along the c axis (Fig. 12c) is expected to increase, and the axial Ni–O(1) bond contract, as the average charge on the A cation decreases. This is indeed seen for $x > 0.6$ but for lower values of x although the La/Sr–O(1) bond lengthens the Ni-O(1) bond length, and tetragonal distortion of the NiO_6 octahedra vary little in comparison with their behavior at higher x values. Despite the increase in average A cation size upon substitution, the mean La/Sr–O bond length decreases linearly with x. The combined decrease in the fourfold La/Sr–O(1) and La/Sr–O(2) bond lengths outweighs the increase in the shortest La/Sr–O(1) bond length. In all cases the trends in La/Sr–O bond lengths at 293 K are mirrored in the low temperature data, with a contraction in all the bond lengths occurring upon cooling to 5 K.

The c/a ratio does show an increase with Sr^{2+} substitution for $0.2 \leq x \leq 0.6$, but the ratio of the axial and equatorial Ni–O bond lengths, a direct measure of the octahedral distortion, does not, the value remaining constant within error over the same composition range. The increase in c/a for $x \leq 0.5$ cannot, therefore, be due to increased Jahn–Teller distortion of the NiO_6 octahedra, but rather to anisotropic expansion of the rock-salt layer and in particular lengthening of the shortest A–O(1) distance parallel to c (see Fig. 8). For $0.6 < x < 1.0$ there is a dramatic decrease in the distortion of the NiO_6 octahedra toward zero due to the combination of a decrease in the axial Ni–O(1) bond length for $x > 0.5$ and an increase in the Ni–O(2) equatorial bond length for $x > 0.6$ (Fig. 10). In this composition range, the changes are exactly mirrored by the lattice parameters: the c lattice parameter decreases for $x > 0.5$ and the a lattice parameter increases for $x > 0.6$, and, as a result, the c/a ratio decreases sharply.

Interpretation of Structural Variations

The variation in the Ni–O distances in the NiO_6 octahedron with x are given in Fig. 10 and Table 2. Fig. 13a shows the mean Ni–O distance and root-mean-square deviation from it while Fig. 13b shows the ratio of the percentge change in the axial and equatorial bond lengths from $x = 0.0$. Much more significant changes occur at and beyond $x = 0.6$. The axial distortion of the octahedra is significantly reduced. This is due to a small *increase* in the equatorial distance on oxidation from 0.6 to 1.0 (the distance remains 2% smaller than at $x = 0.0$) and a pronounced decrease in the Ni–O axial distance. As noted by previous researchers, the c/a ratio is not a good indicator of the evolution of the NiO_6 local environment; the variation in the A–O distances discussed above is also important. These data do, however, reaffirm the original conclusion in the pioneering study by Gopalkrishnan *et al.*—the c/a anomaly at $x = 0.5$ is correlated with a change in the

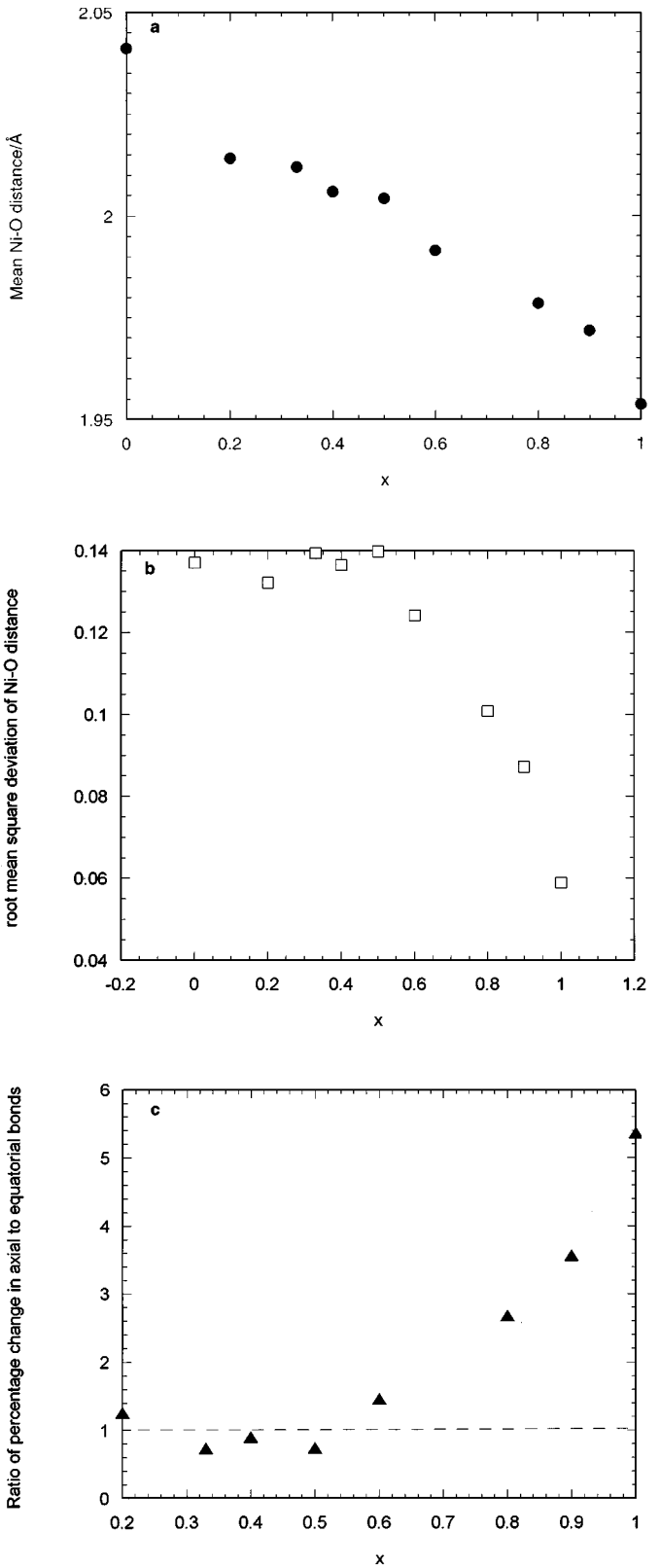

FIG. 13. (a) The mean Ni–O bond length and (b) root mean square deviation from the mean bond length. (c) The ratio of the percentage changes in axial and equatorial bond length from their values at $x = 0.0$.

evolution of the structure of the NiO_6 octahedron with oxidation.

Any discussion of the electronic structure of these phases in terms of Ni–O bond lengths must begin with the marked distortion of the NiO_6 octahedra of the non-Jahn–Teller active cation Ni^{II} found in the $x = 0$ end-member (19). The following analysis is based on the transfer integral/on-site repulsion arguments originally given by Goodenough (51) but modified in the light of more recent high-level band structure calculations (12, 13). The best way to account for the distortion is to note that the material is close to a metal-insulator transition of the Mott–Hubbard type and that the octahedral elongation can arise from a partial breakdown of the high spin $S = 1$ configuration as the majority and minority spin bands overlap at the Fermi level. The electronic configuration can be seen as that of high spin Ni^{II} slightly modified by overlap of the x^2–y^2 spin up (majority spin) band with the z^2 spin down (minority spin) band as shown in Fig. 14a. The bandwidth W and the axial elongation, which stabilize both z^2 majority and minority spins, push some of the z^2 spin down states below E_f. Spin-polarized band structure calculations on La_2NiO_4 in the antiferromagnetically ordered state give an indication of the electronic structure (12, 13), although the inability of such calculations to treat the Mott–Hubbard insulating state must be remembered in dealing with strongly correlated first transition series oxides. In the experimentally observed slightly axially distorted structure treated without spin polarization, both the x^2–y^2 and z^2 bands cut the Fermi level, consistent with the high spin formalism indicated by a simple ionic treatment: the bandwidths are 3.2 and 1.2 eV respectively, reflecting the better overlap of the O $2p$ wavefunctions within the NiO_2 layer with the x^2–y^2 orbital. In the spin-polarized calculation, the splittings of both bands are about 0.5 eV between majority and minority spins. The majority spin z^2 band is full and below E_f: both the majority x^2–y^2 and minority z^2 bands cut the Fermi level, in qualitative agreement with the argument proposed above. The relative occupancies of the z^2 and x^2–y^2 levels are 52 and 48%. Therefore the band structure calculations confirm the qualitative argument given for the distortion in La_2NiO_4, in terms of preferred occupancy of z^2 driven by intraatomic spin polarization, although they fail in detail as the calculations predict metallic behavior. We suggest that the Hubbard U_{inter}, splitting $d^8 + d^8$ states from $d^7 + d^9$, produces a larger subband splitting than indicated by calculation, resulting in a gap opening at E_f for a half-filled situation, as observed experimentally and indicated in Fig. 14b. The states at the top of the upper Hubbard subband will have some z^2 spin down character and therefore the spin state of the Ni^{II} ion is not pure high spin $S = 1$.

This admixture of z^2 minority spin states near E_f followed by a region with greater majority spin x^2–y^2 character can explain the evolution of the NiO_6 octahedron on

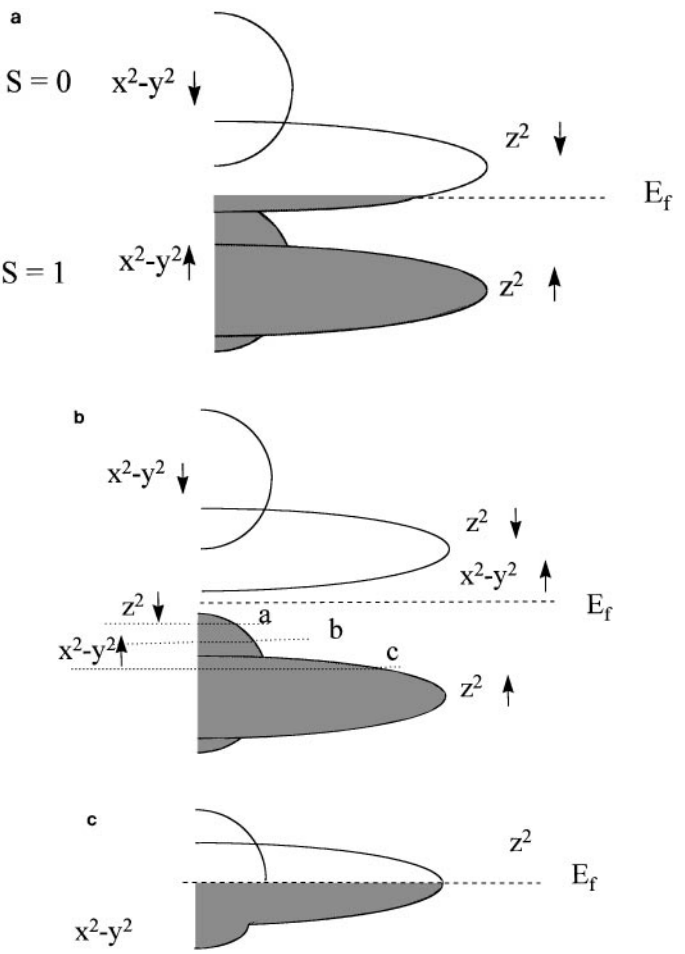

FIG. 14. Density of states in $La_{2-x}Sr_xNiO_4$ derived from the variation in structural behaviour with x. (a) The splitting of the e_g band into low and high spin states plus broadening due to band formation. (b) The extra influence of the interatomic U (Hubbard U) splits the bands in (a) in half: regions a, b, and c correspond to different composition ranges derived from the structural parameters. (c) Density of states beyond $x = 0.8$ when the distortion of the NiO_6 octahedra is sharply reduced. This diagram assumes complete spin polarization which is only indicated for $x = 1.0$ below the magnetic transition temperature of 44 K. Loss of the correlation splitting would lower the Fermi level to one quarter, rather than half-filling but still give equal occupancy of x^2–y^2 and z^2 derived states.

oxidation. From $x = 0.0$ to 0.2, the mean NiO distance decreases sharply and the octahedral distortion is slightly reduced as the antibonding Ni–O σ^* electrons are removed. The holes formed have predominantly z^2 character (indicated as region (a) on Fig. 14b), giving a slightly greater reduction in axial bond length. Over the entire $x = 0.0$–0.6 range, the close proximity between the nickel oxidation state and the bond valence sum indicates that the e_g electrons are localized and, according to detailed studies on $LnNiO_3$ (52), predominantly located on Ni. For $x = 0.2$–0.5 the distortion is slightly but significantly enhanced from the

Ni^{II} case because the percentage contraction in the axial bond is reduced. This is because the holes formed now have more x^2-y^2 character (region (b) in Fig. 14b) as E_f moves into the region of N(E) below the bottom of the minority spin z^2 band and into the majority spin x^2-y^2 states, giving a greater shortening of the equatorial bonds. This would occur immediately upon oxidation in the absence of stabilization of the z^2 spin-down states, as the states near E_f would have predominantly x^2-y^2 character at all d-electron counts due to the greater width of the x^2-y^2 band. In addition, the rigid band approximation can be expected to break down as low spin Ni(III) formed on oxidation is Jahn–Teller unstable and will order the electron in the z^2 orbital. This leaves the hole with predominant x^2-y^2 character, thus changing N(E) from La_2NiO_4 toward further stabilization of the z^2 orbital. The localized nature of the Ni(III) states makes the observed bond lengths an average over Ni(II) and Ni(III) sites. This view of the electronic structure is consistent with the low conductivity and its insensitivity to x across this composition range: the e_g states are still localized at this point as μSR shows that local moments and well-defined magnetic order are still present (21). The octahedral distortion, as indicated by the axial/equatorial ratio and the mean square distortion, is maximized at $x = 0.5$, but the small extent of the distortion is not at all in agreement with total orbital ordering at the Ni(III) centers. A preferrable interpretation is that the occupied states have predominant but not exclusive z^2 character, consistent with the size of the octahedral distortion being only slightly greater than at $x = 0.0$ where it is clearly not attributable to Jahn–Teller considerations. The observation that the extent of octahedral distortion appears to remain constant for $0.2 \leq x \leq 0.5$ despite the increase in concentration of localized low-spin Ni^{III} is somewhat surprising, but can be interpreted in terms of the density of states predicted by modification of band structure calculations on La_2NiO_4.

At $x = 0.6$, the octahedra both contract significantly and become considerably less distorted. The axial and equatorial distances contract from 0.5, but the axial much more strongly, indicating that the holes formed on oxidation here have more z^2 and less x^2-y^2 character. This is consistent with N(E) moving into region (c) in Fig. 14b, where the occupied states have more z^2 character (the retention of the correlation splitting means that these electrons have the majority spin at this point). From $x = 0.6$ to $x = 0.8$, there is a large decrease in the room temperature resistivity and a pronounced contraction of the mean NiO distance. Importantly however, the equatorial Ni–O distance increases slightly while the axial distance decreases strongly. The Ni–O(2) bond lengthens on delocalization, despite the further oxidation of Ni^{II} to Ni^{III} seen both from iodometric analysis and bond valence sum calculations. This is consistent with significant redistribution of the orbital character of the occupied e_g states at this point, indicating that the x^2-y^2 character of the occupied states is significantly increasing and thus that the stabilization of the z^2 orbital is lost to a large extent, producing the situation in Fig. 14c, where the center of the z^2 band is raised toward the Fermi level. This redistribution of orbital occupancy occurs together with a breakdown in the agreement of the bond valence sum (computed with the observed distances) with the formal oxidation state (Fig. 11). We may correlate the considerably increased regularity of the NiO_6 octahedra and the enhanced conductivity with a transition from localized to delocalized in the nature of Ni e_g $3d$ states beyond $x = 1.1$. This will effectively suppress the Jahn–Teller distortion produced by the localized Ni^{III} states and thus considerably reduces the driving force to distinguish between axial and equatorial antibonding character of the e_g states by orbital ordering at the metal site. Much more pronounced octahedral distortions are seen at the localized-insulating transition in CMR manganate oxides, driven by the first-order Jahn–Teller effect at Mn^{III} (53). μSR indicates that local moments and short range static magnetic order persist to $x = 1.0$, so the correlation splitting at each nickel site must be retained, at least below the magnetic transition temperature of 44 K. The most conservative interpretation of the data is thus that this structural change beyond $x = 0.6$ is the result of a change from small (Jahn–Teller active) to large (Jahn–Teller inactive) polaron carriers as a precursor to the metal-insulator transition which occurs beyond $x = 0.6$ (15). The distortion of the octahedron in the Ni(III) phase $LaSrNiO_4$ is still significantly larger than found for $NdSrCrO_4$, indicating that e_g delocalization is incomplete.

The assignment of delocalized electron behavior for $x > 0.6$ is supported by the deviation between the oxidation state and the bond valence sum beyond $x = 0.6$ and is consistent with a change in the electronic structure at the nickel site at this point.

The idea that the e_g states are localized as small polarons before $x = 0.6$ is consistent with the temperature dependence of the bulk structures. The evolution of the average structures at $x = 0.2$–0.4 on cooling are of interest in view of recent reports of the formation of charge-ordered stripe lattices due to the real-space segregation of holes and spins (7, 24, 25). These effects appear to be much more pronounced at $x = 0.33$ than at any other composition in the nickelate series. Single crystal neutron diffraction indicates the formation of a "glassy" phase of uncorrelated stripes at the charge-ordering temperature indicated by specific heat, magnetization, and transport measurements, followed by spin-ordering and the development of long-range charge correlation below 200 K. The microscopic nature of these stripes is still uncertain. It is interesting to consider the anomaly in the thermal evolution of the Ni–O axial bond length and U_{33} parameter of this axial oxygen in the context

of the demonstrated existence of these stripes. The increased axial bond length occurs on cooling from 150 to 100 K, within the ordered array of stripes in phase II identified in Ref. 25, and is also observed for $x = 0.2$ between 300 and 150 K but not at $x = 0.4$. It is consistent with enhanced localization of the e_g electrons between 150 and 100 K at $x = 0.33$ resulting in an enhanced Jahn–Teller distortion. This small anomaly in the bulk structure may be as a result of orbital ordering at Ni^{III} in the charge ordered state. The observed bond length anomalies are a small effect but are consistent with the behavior at the metal-insulator transition of $LnNiO_3$ perovskites (52). The metal-insulator transitions in the Ni(III) $LnNiO_3$ perovskites occur with a small isotropic increase in the Ni–O distances of the order of 0.004 Å (52) which drives an increase in cell volume. In this case the volume decrease of $x = 0.33$ on cooling from 150 to 90 K is anomalously small. The absence of sharp metal-insulator transitions in the present layered materials can be correlated with the more subtle nature of this structural transition, which only involves elongation of the axial Ni–O distance while the equatorial bond continues to contract, resulting in a less pronounced increase in the unit cell volume. The disappearance of the stripes appears correlated with the decreased octahedral distortion interpreted as a transition between small and large polarons.

Phase Segregation and Inhomogeneity at $x = 1.0$

Investigations into the structure of the $x = 1.0$ composition, $LaSrNiO_{4+\delta}$, are complicated by the occurrence of multiphasic behavior for samples prepared at 1250°C under 1 atmosphere O_2. These synthesis conditions are very commonly used in the literature, with only Ref. 2 using a significantly higher synthesis temperature of 1375°C. The signature of the phase segregation in the powder diffraction pattern is the presence of broad features associated with the Bragg reflections, with no systematic *hkl* dependence, which cannot be described using a single phase model. The multiphasic nature is enhanced for samples subsequently annealed at low temperatures, but reduced for samples annealed at 1450°C, where the use of *hkl* dependent anisotropic line broadening across the pattern is sufficient to model the observed profile. The $x = 0.8$ and 0.9 samples display analogous broadening but at a greatly reduced level. In view of these observations it is concluded that an inhomogeneous distribution of A cations within the sample at the $x = 1.0$ composition is responsible for the behavior encountered. The reconciliation of the global composition with those of the three phases, as derived from the c/a ratio, confirms this view. The bond valence sum for the majority (79.8%) phase appears to agree with this assignment of compositions, the value of 2.702 being reasonably consistent with that obtained for the single phase $x = 1.0$ sample synthesized at 1450°C (2.669).

The majority phase contains an approximately equimolar ($x = 0.99$), homogeneous distribution of La/Sr, but fluctuations in the La/Sr ratio within the sample lead to the coexistence of two strontium-rich phases such that the overall stoichiometry of $LaSrNiO_{3.955}$ is retained, resulting in the abnormal peak shape features found in the neutron diffraction data. The influence of the anisotropic strain and peak displacement parameters on the quality of fit indicates the extent of La/Sr inhomogeneity within the sample after reaction at 1250°C. The derived x values should thus be thought of as representing maxima in a broad distribution of La/Sr ratios between 0.99 and 1.16 rather than discrete phases formed by thermodynamic phase separation. The observation of significant anisotropic broadening and peak displacement not observed under the same synthetic conditions for smaller values of x indicates that the La/Sr segregation becomes more significant as x increases. The partial alleviation of the profile problems for $x = 1.0$ samples prepared at 1450°C rather than 1250°C, but their augmentation for samples annealed at lower temperatures, 500°C (1 atmosphere O_2) and 400°C (285 atmospheres of O_2) (Fig. 4), is consistent with this view. Annealing the sample at higher temperature, and thereby increasing the rate of diffusion within the solid, leads to a more uniform distribution of the two A cations and the concomitant absence of truly multiphasic behavior. The enhanced extent of phase-separation at lowest temperatures and under higher pressures of oxygen can be correlated with enhanced stabilization of strontium rich Ni(IV) containing regions (produced by the cation inhomogeneity) as the pressure of oxygen increases. Low temperature anneals of samples with inherent La/Sr inhomogeneity further enhance phase segregation, as cation diffusion is not possible and presumably the oxide anion distribution rearranges to match the cation inhomogeneity. However, *hkl* dependent line broadening analysis is still required to fit the TOF diffraction profile of the 1450°C sample, indicative of residual strain effects resulting from fluctuations in the La/Sr ratio over a shorter length scale than that corresponding to phase segregation.

The observation of such anisotropic broadening of the Bragg reflections in the $La_{2-x}Sr_xNiO_4$ series has been reported previously by Sreedhar *et al.* (15) but no explanation for the broadening of the reflections, especially $\{00l\}$, for samples with high strontium contents was proposed. All these observations are consistent with the conclusion that peculiarities encountered for $x = 1.0$ are due to fluctuations in the La/Sr ratio across the sample and that the multiphasic behavior is inextricably correlated with the precise oxygen content of the materials. These observations are of importance in the interpretation of the behavior of this and other nickelate systems, especially with respect to the comparison of properties with those of the isostructural high T_c cuprates.

The observation of phase separation in this case is of interest in comparison with the well-defined increased difficulty in preparing single phases of $La_{2-x}Sr_xCuO_4$ beyond $x = 0.2$ (54, 55), consistent both with the idea that $La_{2-x}Sr_xCuO_4$ is not stable below 1100°C and with the idea that reaction kinetics are sluggish. Our high temperature synthesis involves furnace cooling through lower temperatures so thermodynamic instability is not established here, but increasingly sluggish kinetics are. The influence of thermodynamics is not ruled out.

CONCLUSION

Detailed neutron powder diffraction measurements show that the NiO_6 octahedron in $La_{2-x}Sr_xNiO_4$ undergoes a complex evolution with increasing nickel oxidation state, consistent with the orbital nature of the density of states function in the e_g band split by both inter- and intraatomic correlation energies and Jahn–Teller considerations. The pronounced loss of the local distortion at the x value where the electrical conductivity increases sharply and charge-order/stripe instabilities are suppressed is consistent with the delocalization of the e_g electrons at this composition, also indicated by the deviation of the nickel valence derived from the bond lengths from the measured oxidation state. The anomaly in c/a is due to the interplay between the variation in the La/Sr distance to the axial oxide and the evolution of the NiO_6 octahedron. The present results clearly show an anomaly in the Ni environment directly correlated with the reported transport anomaly, indicating that electron–phonon coupling and polaronic effects can be expected to be much more significant in the nickelates than the analogous cuprates. This correlation of octahedral distortion with the change in transport properties correlates with theoretical (28, 56) and experimental (3, 57) evidence for stronger electron–phonon coupling in the nickelates.

The $x = 1$ composition had been reported previously to display anomalous anisotropic broadening of the Bragg reflections with $l \neq 0$ (15). Here we demonstrate that this is due to segregation into slightly Sr deficient majority phase and two Sr-rich minority phases under the commonly used synthesis conditions. The minority phases are highly strained. The behavior of the phase-separation on annealing suggests that cation inhomogeneity can be removed at high temperature but is accentuated at lower temperatures or higher oxygen pressures, perhaps due to stabilization of the strontium-rich regions. Considerable care in synthesis in the large x region is required to establish the intrinsic properties of this family.

ACKNOWLEDGMENTS

MJR thanks the U.K. EPSRC and the Petroleum Research Foundation of the American Chemical Society for support of this work.

REFERENCES

1. Y. Takeda, R. Kanno, M. Sakano, O. Yamamoto, M. Takano, Y. Bando, H. Akinaga, and K. Takita, J. B. Goodenough, *Mater. Res. Bull.* **25,** 293 (1990).
2. R. J. Cava, B. Batlogg, T. T. M. Palstra, J. J. Krajewski, W. F. Peck, A. P. Ramirez, and L. W. Rupp, *Phys. Rev. B* **43,** 1229 (1991).
3. T. Strangfeld, K. Westerholt, and H. Bach, *Physica C* **183,** 1 (1991).
4. M. Kato, Y. Maeno, and T. Fujita, *Physica C* **176,** 533 (1991).
5. C. H. Chen, S.-W. Cheong, and A. S. Cooper, *Phys. Rev. Lett.* **71,** 2461 (1993).
6. X. Granados, J. Fontcuberta, M. Vallet-Regi, M. J. Sayagues, and J. M. Gonzalez-Calbet, *J. Solid State Chem.* **102,** 455 (1993).
7. S.-W. Cheong, H. Y. Hwang, C. H. Chen, B. Batlogg, L. W. Rupp, and S. A. Carter, *Phys. Rev. B* **49,** 7088 (1994).
8. V. Sachan, D. J. Buttrey, J. M. Tranquada, J. E. Lorenzo, and G. Shirane, *Phys. Rev. B* **51,** 12742 (1995).
9. E. Pellegrin, J. Zaanen, H. J. Lin, G. Meigs, C. T. Chen, G. H. Ho, H. Eisaki, and S. Uchida, *Phys. Rev. B* **53,** 10667 (1996).
10. M. Medarde and J. Rodriguez-Carvajal, *Z. Phys. B* **102,** 307 (1997).
11. J. G. Bednorz and K. A. Muller, *Z. Phys. B* **64,** 189 (1996).
12. G. Y. Guo and W. M. Temmerman, *Phys. Rev. B* **40,** 285 (1989).
13. G. Y. Guo and W. M. Temmerman, *J. Phys. C* **21,** L803 (1988).
14. T. R. Thurston, R. J. Birgeneau, M. A. Kastner, N. W. Preyer, G. Shirane, Y. Fujii, K. Yamada, Y. Endoh, K. Kakurai, M. Matsuda, Y. Hidaka, and T. Murakami, *Phys. Rev. B* **40,** 4585 (1989).
15. K. Sreedhar and J. M. Honig, *J. Solid State Chem.* **111,** 147 (1994).
16. J. Gopalakrishnan, G. Colsmann, and B. Reuter, *J. Solid State Chem.* **22,** 145 (1977).
17. C.-J. Liu, M. D. Mays, D. O. Cowan, and M. G. Sanchez, *Chem. Mater.* **3,** 495 (1991).
18. K. Sreedhar and C. N. R. Rao, *Mater. Res. Bull.* **25,** 1235 (1990).
19. J. Rodriguez-Carvajal, M. T. Fernandez-Diaz, and J. L. Martinez, *J. Phys.* **3,** 3215 (1991).
20. G. Aeppli and D. J. Buttrey, *Phys. Rev. Lett.* **61,** 203 (1988).
21. K. H. Chow, P. A. Pattenden, S. J. Blundell, W. Hayes, F. L. Pratt, T. Jestadt, M. A. Green, J. E. Millburn, M. J. Rosseinsky, B. Hitti, S. R. Dunsiger, R. F. Kiefl, C. Chen, and A. J. S. Chowdhury, *Phys. Rev. B* **53,** 14725 (1996).
22. A. P. Ramirez, P. L. Gammel, S. W. Cheong, D. J. Bishop, P. Chandra, *Phys. Rev. Lett.* **76,** 447 (1996).
23. H. Kuwahara, Y. Tomioka, Y. Moritomo, A. Asamitsu, M. Kasai, R. Kumai, and Y. Tokura, *Science* **272,** 80 (1996).
24. J. M. Tranquada, D. J. Buttrey, and V. Sachan, *Phys. Rev. B* **54,** 12318 (1996).
25. S. H. Lee and S. W. Cheong, *Phys. Rev. Lett.* **79,** 2514 (1997).
26. J. E. Greedan, G. Liu, B. W. Arbuckle, K. V. Ramanujachary, and M. Greenblatt, *J. Solid State Chem.* **97,** 419 (1992).
27. J. M. Tranquada, D. J. Buttrey, V. Sachan, and J. E. Lorenzo, *Phys. Rev. Lett.* **73,** 1003 (1994).
28. J. Zaanen and P. B. Littlewood, *Phys. Rev. B* **50,** 7222 (1994).
29. M. Beltran, J. M. Dominguez, A. Montoya, G. Tavizon, L. Vincente, and T. Viveros, *Catal. Lett.* **15,** 199 (1992).
30. P. J. Heaney, A. Mehta, G. Sarosi, V. E. Lamberti, and A. Navrotsky, *Phys. Rev. B* **57,** 10370 (1998).
31. H. M. Rietveld, *J. Appl. Crystallogr.* **2,** 65 (1969).
32. P. J. Brown and J. M. Matthewman, Rutherford Appleton Laboratory, 1987.
33. P. J. Brown and J. M. Matthewman, Rutherford Appleton Laboratory, 1990.
34. P. J. Brown and J. M. Matthewman, Rutherford Appleton Laboratory, 1993.
35. W. I. F. David, D. E. Akporiaye, R. M. Ibberson, and C. C. Wilson, Rutherford Appleton Laboratory, 1988.

36. A. C. Larson and R. B. Von Dreele, "General Structural Analysis Systems" (A. C. Larson, and R. B. Von Dreele, Eds.), Los Alamos National Laboratory, 1994.
37. J. D. Jorgensen, B. Dabrowski, S. Pei, D. R. Richards, and D. G. Hinks, *Phys. Rev. B* **40,** 2187 (1989).
38. P. Ganguly and C. N. R. Rao, *J. Solid State Chem.* **53,** 193 (1984).
39. K. Sander, U. Lehmann, and H. Muller-Buschbaum, *Z. Anorg. Allg. Chem.* **480,** 153 (1981).
40. R. Benloucif, N. Nguyen, J. M. Greneche, and B. Raveau, *J. Phys. Chem. Solids* **52,** 381 (1991).
41. R. T. Shannon and C. T. Prewitt, *Acta Crystallogr. B* **25,** 925 (1969).
42. R. T. Shannon and C. T. Prewitt, *Acta Crystallogr. B* **26,** 1046 (1970).
43. R. T. Shannon and C. T. Prewitt, *Acta Crystallogr. A* **32,** 751 (1976).
44. G. Demazeau, M. Pouchard, and P. Hagenmuller, *J. Solid State Chem.* **18,** 159 (1976).
45. I. D. Brown and R. D. Shannon, *Acta Crystollagr. A* **29,** 266 (1973).
46. I. D. Brown and D. Altermatt, *Acta Crystallogr. B* **41,** 244 (1985).
47. G. Demazeau, A. Marbeuf, M. Pouchard, and P. Hagenmuller, *J. Solid State Chem.* **3,** 582 (1971).
48. A. Wichainchai, P. Dordor, J. P. Doumerc, E. Marquestaut, M. Pouchard, and P. Hagenmuller, *J. Solid State Chem.* **74,** 126 (1988).
49. G. Demazeau, M. Pouchard, and P. Hagenmuller, *J. Solid State Chem.* **18,** 159 (1976).
50. N. Brese and M. O'Keefe, *Acta Crystollagr. B* **47,** 192 (1991).
51. J. B. Goodenough and S. Ramashesha, *Mater. Res. Bull.* **17,** 383 (1982).
52. J. L. Garcia-Munoz, J. Rodriguez-Carvajal, P. Lacorre, and J. B. Torrance, *Phys. Rev. B* **46,** 4414 (1992).
53. P. G. Radaelli, G. Iannone, M. Marezio, H. Y. Hwang, S.W. Cheong, J. D. Jorgensen, and D. N. Argyriou, *Phys. Rev. B* **56,** 8265 (1997).
54. P. G. Radaelli, D. G. Hinks, A. W. Mitchell, B. A. Hunter, J.L. Wagner, B. Dabrowski, K. G. Vandervoort, H. K. Viswanathan, and J. D. Jorgensen, *Phys. Rev. B* **49,** 4163 (1994).
55. K. Yoshimura, H. Kubota, H. Tanaka, Y. Date, M. Nakanishi, T. Ohmura, N. Saga, T. Sawamura, and T. Uemura, *J. Phys. Soc. Japan* **62,** 1114 (1993).
56. V. I. Anisimov, M. A. Korotin, J. Zaanen, and O. K. Andersen, *Phys. Rev. Lett.* **68,** 345 (1992).
57. X. X. Bi, P. C. Eklund, and J. M. Honig, *Phys. Rev. B* **48,** 3470 (1993).